Faculty of Science

Magmatic fractionation of trace elements in biotite with emphasis on indium in the Salmi batholith, Russian Karelia

Alice Bäckström

Degree of Bachelor of Science
with a major in Earth Sciences
15 hec

Department of Earth Sciences
University of Gothenburg
2020 B-1088

UNIVERSITY OF GOTHENBURG

UNIVERSITY OF GOTHENBURG
Department of Earth Sciences
Geovetarcentrum/Earth Science Centre

Magmatic fractionation of trace elements in biotite with emphasis on indium in the Salmi batholith, Russian Karelia

Alice Bäckström

ISSN 1400-3821

B1088
Bachelor of Science thesis
Göteborg 2020

Mailing address
Geovetarcentrum
S 405 30 Göteborg

Address
Geovetarcentrum
Guldhedsgatan 5A

Telephone
031-786 19 56

Geovetarcentrum
Göteborg University
S-405 30 Göteborg
SWEDEN

Sammanfattning

Biotit är ett av det vanligaste ferromagnesiska mineralen i graniter och dess kristallstruktur är även gynnsam för ett flertal katjons substitutioner. Tack vare mineralets förmåga att uppta olika katjoner kan bergets kemi, processer i berget och lokala metallanrikningar i berget återspeglas i biotitens spårelementsmönster. Biotit är också ett mineral som har visat sig med fördel uppta indium. Indium är en betydelsefull metall för att utveckla den gröna tekniken och utgör en viktig komponent i till exempel solpaneler. Anrikningar av indium har hittats kopplade till rapakivi graniter i södra Finland och i Karelin, västra Ryssland. I detta arbete analyseras spår- och huvudelement i biotit kommande från Salmi batoliten, en rapakivi-intrusion kopplad till indiumanrikningar. Spår- och huvudelement uppmätas med hjälp av *laser ablation inductive coupled plasma mass spectrometer* (LA-ICP-MS) för att utvärdera hur dessa element påverkas av fraktionering i biotit. Arbetet utvärderar också användandet av biotit som ett spårmineral för att hitta lokala metallanrikningar med fokus på indium, det innehåller även petrografiska beskrivningar av fem granit typer från Salmi batoliten. De petrografiska beskrivningarna visar att graniterna från den inre delen av batoliten kan särskiljas från graniterna tillhörandes dess yttre delar. Analyserna av elementmönstren i biotiten visar att andelen Li och ^{IV}Al ökar i mineralets kristallstruktur med ökad fraktionering av värdberget. Även andelen ten i biotiten påverkas av fraktioneringsprocessen och är högre i de mer fraktionerade graniterna. Analysen av indium visar på att metallen med fördel tas upp av biotit och/eller amfibol när mineralet finns närvarande, men metallen påverkas inte av fraktionerings processen i batoliten och ingen anrikning av indium är synlig i biotiten. Tillskillnad från detta kan den tydliga ökningen av andelen ten i biotiten peka på en anrikning av metallen i batoliten.

Nyckelord: Biotit, Spårämnen, LA-ICP-MS, Glimmer klassifikation, Indium, Rapakivi graniter, Spårmineral.

Abstract

Biotite is one of the most common ferromagnesian phases in granitic systems and has a crystal lattice allowing for a range of cation substitutions. The mineral can record whole rock chemistry, mirror processes in the rocks and indicate local metal enrichments. Biotite is thought to be a mineral preferentially incorporating indium which is a key metal for green technology such as solar panels. Indium enrichments have been found to be connected to rapakivi granites in southern Finland and western Russian Karelia. This thesis contains trace- and major element analyses of biotite collected from the Salmi rapakivi batholith in Russian Karelia which is connected to indium enrichments. The analyses are done by laser ablation inductive coupled plasma mass spectrometry (LA-ICP-MS) for evaluating the element behavior during magmatic fractionation in biotite. The use of biotite as an exploration vector for certain metals with emphasis on indium is also discussed as well as petrographic thin section descriptions of five granite types within the Salmi rapakivi batholithh. The petrography shows that the granite types from the inner part of the batholith exhibits textural similarities and can be discriminated from the granites in the more distant parts of the batholith. During magmatic fractionation the incorporation of Li into biotite is increasing as well as the amount of ^{VI}Al. The tin grades in biotite is also strongly affected by the fractionation process. Indium is found to be preferentially incorporated into biotite and/or amphibole if present, but indium is not seen to be affected by the fractionation process. In the biotite, no indium enrichment is identified thus the use of biotite as an exploration vector for the metal cannot be supported. But the clear enrichment of Sn displayed by biotite may be used in mineral exploration.

Keywords: Biotite, Trace elements, LA-ICP-MS, Mica classification, Indium, Rapakivi granites, Exploration vectors.

Table of Contents

Introduction

Micas are major phases in both igneous and metamorphic rocks and have wide stability fields over different temperatures and pressures. The crystal structure of mica are also seen to allow for a considerable range of trace element incorporations (Tischendorf et al., 2001). Trace elements in trioctahedral mica (biotite group) have been used in numerous studies to provide information about pressure-temperature conditions during metamorphism of host rocks, fractionation patterns in intrusive rocks, magmatic evolution and others (Ballouard et al., 2020; Simons et al., 2017; Tischendorf et al., 2001). Biotite composition is thought to reflect element concentrations in the host rock and can thus be used to extract petrogenetic information. Trace element patterns in biotite is therefore very useful in evaluating host rock chemistry and could also be used for understanding important element behaviour during magmatic fractionation.

Other articles have also investigated the usage of biotite as an indicator mineral for finding metal enrichments (Tischendorf et al., 2001; Warren et al., 2015). Biotite is thought to mirror metal concentrations in the host rock and can therefore be used to find deviating high metal concentrations.

The analysed biotite in this work is collected from the Salmi rapakivi batholith located in Russian Karelia. The batholith show a clear fractionation trend between the comprising granites and are associated with several metal enrichments such as Sn, In and Mo in the most evolved areas (Valkama et al., 2016b),(Sundblad, K. personal communication).

Indium is suggested to preferable be incorporated into ferromagnesian phases like biotite (Knighton, 2015; Wager et al., 1958). A limited amount of studies has measured indium abundance in biotite and no study has evaluate biotite as a pathfinder mineral for indium.

Indium is an important key metal in the production of touchscreens, television screens and solar panels. The expanded need for these products has increased the demand on reliable indium supplies. China (40%) and the Republic of Korea (32%) stands for the world's major production of indium (U.S Geological Survey, 2020). The refinery production of indium is also dependent on the world's zinc production from sphalerite ores, because the mineral is one of the most important indium-carrier. (Broman et al., 2018)

Because of the few countries who dominate the indium market, its dependency on zinc production and the metal's economic importance for future technologies, the European Union have classified indium as a critical raw material (European Commission, 2014). The European Union consider indium as an important raw material for EU's economy, but the supply is associated with risks. European commission's classification shed light upon the increased need for finding new indium mineralizations that are reliable.

This thesis will be focusing on the behaviour of trace elements in biotite in magmatic fractionation and also evaluate if biotite can be used as a pathfinder mineral in mining-exploration with emphasis on indium. Trace- and major element data for biotite is used, measured by laser ablation inductively coupled plasma mass spectrometer (LA-ICP-MS). Furthermore, petrographic thin section descriptions are also provided for the analysed samples.

Mineral chemistry of Mica

Micas are sheet silicates composed of two tetrahedral layers (T) and one octahedral layer (O) in a TOT+c structure (c = monovalent cation interlayer). Divalent cation substitution (e.g, Fe^{2+}, Mg^{2+}, Zn^{2+} and Cu^{2+}) take place in the octahedral layer and, in the interlayer monovalent cations (e.g, Na^{+}, Ca^{+}, Ba^{+} and Li^{+}) can substitute for K^{+} (Warren et al., 2015).

Micas are divided into two main crystal structure groups, trioctahedral and

dioctahedral, depending on the elements occupying the sites between the OH^- anionic groups in the octahedral layer. Trioctahedral mica include the biotite group and have three out of three places filled in the octahedral sites ideally with Mg^{2+} or Fe^{2+}. In dioctahedral mica, Al^{+3} is occupying two out of three sites, leaving a vacancy in the octahedral layer. This is the crystal structure for mica belonging to the phengite group (e.g. muscovite)(Nesse, 2012).

Cation exchange in trioctahedral mica (biotite group) are mainly controlled by ionic radius, ionic charge and how the occupancy site can adapt to the new replacing cation (Hazen and Wones, 1972; Tischendorf et al., 2001; Volfinger and Robert, 1980).

Depending on the cation substitution in the octahedral layer, micas can also be divided into subgroups classified upon the amounts of Fe_{tot}, Mg^{2+}, Mn^{2+}, Ti^{2+}, ^{VI}Al and Li^{2+} in the octahedral sites. The subdivision used in this thesis is based on the variables *feal* (Fe_{tot} + Mn + Ti – ^{IV}Al) and *mgli* (Mg – Li) presented by Tischendorf et al. (1997).

The evolution of mica within mantle-derived magmatic rocks are the series from phlogopite to annite, with an increase of Fe and a depletion of Al. The fractionation trend visible for mica in crustal derived magmatic rocks are going from annite towards polylithionite with an increase in Li. (Tischendorf, 2007). Highly fractionated pegmatites in Norway is also showed to contain Li-rich siderophyllite and polylithionite (Rosing-Schow et al., 2018).

Indium

Indium mineralizations are rare and the estimated abundance in the continental crust is around 0,05 ppm. The metal is classified as a chalcophile element and is mostly trivalent in an oxidized state. During mantle melting, indium behaves as a moderately incompatible element and will preferentially be concentrated in the melt. Indium is mostly found as a trace element in other minerals (e.g biotite and amphibole) and, in important economic mineralizations indium substitute for base-metals in sulphide minerals. Indium is mainly associated with elements such as zinc, copper and tin and important indium-carriers are therefore sphalerite (ZnS), chalcopyrite ($CuFeS_2$) and stannite (Cu_2FeSnS_4). In rare cases when indium concentrations are highly elevated the element can form its own mineral phase like roquesite ($CuInS_2$), sakuraiite ($(Cu,Zn,Fe)_3(In,Sn)S_4$) or indite ($FeIn_2S_4$) (Schwarz-Schampera and Herzig, 2002).

Literature review

Partition coefficient of indium in biotite, amphibole and in the vapor/melt phase

How indium behaves in magmatic and hydrothermal systems is not fully understood. A recent experimental study was published by Gion et al. (2018) on indium partition coefficient in biotite, amphibole and between the vapor/melt phase, providing possible constrains on the behaviour of indium in magmatic systems.

Indium is preferentially incorporated into ferromagnesian minerals such as biotite and amphibole in felsic magmatic systems (Wager et al., 1958). Gion et al. (2018) suggested a range for $D_{In}^{Bt/melt}$ (partition coefficient for Indium between biotite and melt) between 0,6 ± 0,1 to 16 ± 3, with the main controlling factors for $D_{In}^{Bt/melt}$ to be: (1) the mole fraction of annite, (2) amount of tetrahedral Al and (3) to some extent the amount of Ti.

With an increase in the mole fraction of annite, (the iron-endmember of biotite) and with an increase of tetrahedral Al, $D_{In}^{Bt/melt}$ will decrease. Giving that biotite with a composition closer to phlogopite (the magnesium-endmember of biotite) will have a higher $D_{In}^{Bt/melt}$.

The presence of Ti will lower the amount of indium incorporated into biotite and thus decrease $D_{In}^{Bt/melt}$.

Further thermodynamic evaluation is also indicating that $D_{In}^{Bt/melt}$ depend on f_{H2O}^{vapor} and the activity of K-feldspar.

The $D_{In}^{Amp/melt}$ is calculated by Gion et al. (2018) to range between 25 to 50 with an average of 36 ± 4. The partition coefficient is not thought to vary with the composition of amphibole, but the evaluation of thermodynamics show that $D_{In}^{Amp/melt}$ is dependent on the activities of enstatite, diopside and anorthite as well as the water fugacity (Gion et al., 2018).

Gion et al. (2018) suggested a range of 2,7 to 31 with a mean of 17 ± 5 for the partition coefficient of indium between vapor and melt. $D_{In}^{vapor/melt}$ is implied to may be affected by the amount of chlorine in the hydrothermal solution. The suggestion is consistent with other experimental work showing that chloride complexes are preferable transport agents for In in the fluid phase (Seward et al., 2000). Additionally Broman et al. (2018) indicated that the accumulation of metals (including In) in vein system depends on the abundance of chloride as an transporting complex in the aqueous solution. Summarising, if chloride is present in the fluid phase $D_{In}^{vapor/melt}$ is thought to increase.

Constrains on indium mineralizations

Indium enrichments occur within a large variety of ore deposits such as polymetallic vein-systems, volcano massive sulphide deposits, SEDEX deposits, porphyry copper deposits, and skarn deposits (Schwarz-Schampera and Herzig, 2002). Common for all of the above is an ore-forming process including metal-rich aqueous solutions.

In granitic systems, the exsolution of indium-rich fluids is thought to be related to the ferromagnesic assemblage (Gion et al., 2019). Indium has a high partition coefficient in biotite and amphibole giving the possibility for these phases to control the indium grades in the melt (Gion et al., 2018).

I-type granites crystallizes both biotite *and* amphibole as the primary ferromagnesic phases lowering the ability for exsolving indium enriched fluids (Gion et al., 2019).

S-type granites crystallizes *only* biotite as the primary ferromagnesic mineral whereas A-type granites are primarily crystallizing biotite but can in some cases also crystallize amphibole. Hence biotite is the only main ferromagnesic mineral, having a lower indium partition coefficient compared to amphibole, the possibility for indium enrichments increases. S-type granites compared to amphibole-crystallizing I-type granites are therefore more likely to form indium enrichments. When A-type granites only crystallize biotite, they can be compared with S-types; but if amphibole is present, they behave similar to I-type granites (Gion et al., 2019).

Another controlling factor for the formation of indium mineralizations and the crystallization of roqeusite, the most important indium phase, is the availability of zinc. Sphalerite is the most important indium carrier in In-rich deposits and veins; therefore, the abundance of Zn controls the crystallization of indium phases. If Zn is abundant creating a low In/Zn ratio, large amount of sphalerite will crystallize and hold a large capacity of hosting available In and thus hinder the formation of roqeusite. With a higher In/Zn ratio the low amount of crystallizing sphalerite will reach In saturation early and allowing for roqeusite to form. (Cook et al., 2011).

The usage of biotite as an exploration vector

Because of biotite's ability to reflect the overall chemistry in the host rock, local metal enrichments are thought to be visible in the trace element pattern of the mineral.

The ability of biotite to act as a pathfinder mineral for sulphide deposits with Cu, Ni and Cr was investigated by Warren et al. (2015) in the Sudbury igneous complex in Ontario Canada.

Warren et al. (2015) presented an increased Cu concentration in biotite correlated with an increase of chalcopyrite in the rock, hence the Cu in biotite is seen to increase with proximity to the mineralization.

Ni and Cr variations in biotite could not be correlated with proximity to the mineralization, but the Ni/Cr ratio is seen to increase with a decrease in distance to the sulphide mineralization (Warren et al., 2015).

Warren et al. (2015) concluded that biotite grains associated with sulphide mineralized lithologies could be segregated from biotite connected to barren lithologies.

Tott et al. (2019) published a similar article on the usage of ferromagnesic silicates and oxides as exploration vectors for finding metamorphosed sedimentary exhalative deposits (SEDEX). The study focused on the metamorphosed sediment hosted Pb-Zn-Ag-(Cu-Au) deposit in the Cambrian Kanmantoo group in southern Australia.

Zinc and lead concentrations were found to be elevated in the biotite from rocks closer to the ores and rocks associated with the deposits compared to country rock biotite (Tott et al., 2019). Opposing the findings of Warren et al. (2015), where Cu in biotite is seen to increase with decreasing distance to sulphide mineralizations, Tott et al. (2019) showed that Cu in biotite from the analysed rocks in the Cambrian Kanmantoo group did not show a correlation with proximity to sulphides.

Geological Background

Rapakivi granites

Rapakivi granites have been identified in almost every old crustal area. They often exhibit a rapakivi texture with ovoidal phenocrysts of K-feldspar un-mantled or mantled by plagioclase and a two-generation growth of quartz and K-feldspar (Rämö and Haapala, 2005). Rapakivi granites formed from several magmatic episodes mainly during the Proterozoic eon, but Archean and Phanerozoic rapakivi granites are also identified (Haapala and Rämö, 1999).

Rapakivi complexes are formed in anorogenic settings by bimodal magmatism. (Haapala and Rämö, 1999). Felsic rapakivi magmas are created as a result of partial melting of the crust which is caused by magmatic underplating created by mafic magmas formed form partial melts of the mantle. Rapakivi plutons consists of several types of granitic rocks, with the crystallizing sequence of (1) fayalite-hornblende granite, (2) hornblende granite, (3) biotite-hornblende granite, (4) biotite granite and (5) alkali-feldspar granite associated with accessory topaz (Rämö and Haapala, 2005).

The chemical characteristics of rapakivi granites are variable. Classic Proterozoic rapakivi granites crystallizes from hot-dehydrated magmas with low oxygen fugacity and a high content of Fluorine, alkalis and high field strength ions (HFS) (Haapala and Rämö, 1999; Larin, 2009). But in addition to this, other rapakivi complexes have been interpreted to crystallize under conditions with high water content and high oxygen fugacity (Calzia and Rämö, 2005; Larin, 2009).

The geochemistry of Proterozoic rapakivi granites classify them as A-type granites (anorogenic). The formation of A-type granites is associated with continental rifting and zones of uplift. They have high silica content, are sub- to peralkaline and anhydrous. They are enriched in halogens, HFS and have high Fe/Mg–ratios and a small difference in concentration between LREE and HREE (Winter, 2014).

During the late 20th century the metal fertility of rapakivi granites where discovered. Proterozoic rapakivi granites are associated with (1) hydrothermal Sn-polymetallic greisen- vein-type deposits related to alkali-feldspar, topaz bearing granites in Rondônia and Amazonas in Brazil, southern Finland, south-eastern Missouri, India and Ukraine. (2) Skarn-type

deposits with Sn-W-Be-Zn-Cu-Pb in Pitkäranta, Russia. (3) Fe oxide-Cu-(U-Au-Ag) in southern Australia and south-eastern Missouri (Haapala, 1995). High Indium grades are also found to be connected to greisen vein systems in rapakivi granites in the Fennoscandian shield (southern Finland and Russia Karelia) with possible economic importance (Valkama et al., 2016a; Valkama et al., 2016b).

Study area

The Salmi rapakivi batholith

The batholith is 4 000 km^2 in size and situated north of Lake Ladoga in western Russia Karelia (fig. 1). The batholith is part of an NW-SE trending complex comprised of Mesoproterozoic anorthosite–mangerite–charnokite–granite plutons and is a result of several magma pulses (Amelin et al., 1997). The emplacement took place between 1532 – 1545 Ma (Amelin et al., 1997). The oldest parts of the batholith are located in the south-east corner, and the granites in the batholith becomes younger towards the north-west (Amelin et al., 1997).

The batholith is assumed to be a sheet-like body emplaced at sallow depth. The thickness of the intrusion increases from north-west (2-5 km) to the central parts (10km) and with the thickest area in the south-eastern part (>10 km) where the feeder channel is presumed to be placed (Amelin et al., 1997)

The dominant rock type is hornblende–biotite rapakivi granite. The rapakivi granites in the batholith can be divided into four textural groups: (1) coarse-grained granite with plagioclase mantled K-feldspar or unmantled K-feldspar; (2) porphyritic granite with fine-grained groundmass; (3) coarse-grained granite; (4) aplitic granite dikes (Amelin et al., 1997). The coarse-grained granites with rapakivi texture comprise the batholith's south-east and central parts and becomes replaced with finer grained textures towards the batholith's north-western margin (Metso, 2018)

A fractionation zoning from south-east to north-west is visible in the granites comprising the batholith. This type of

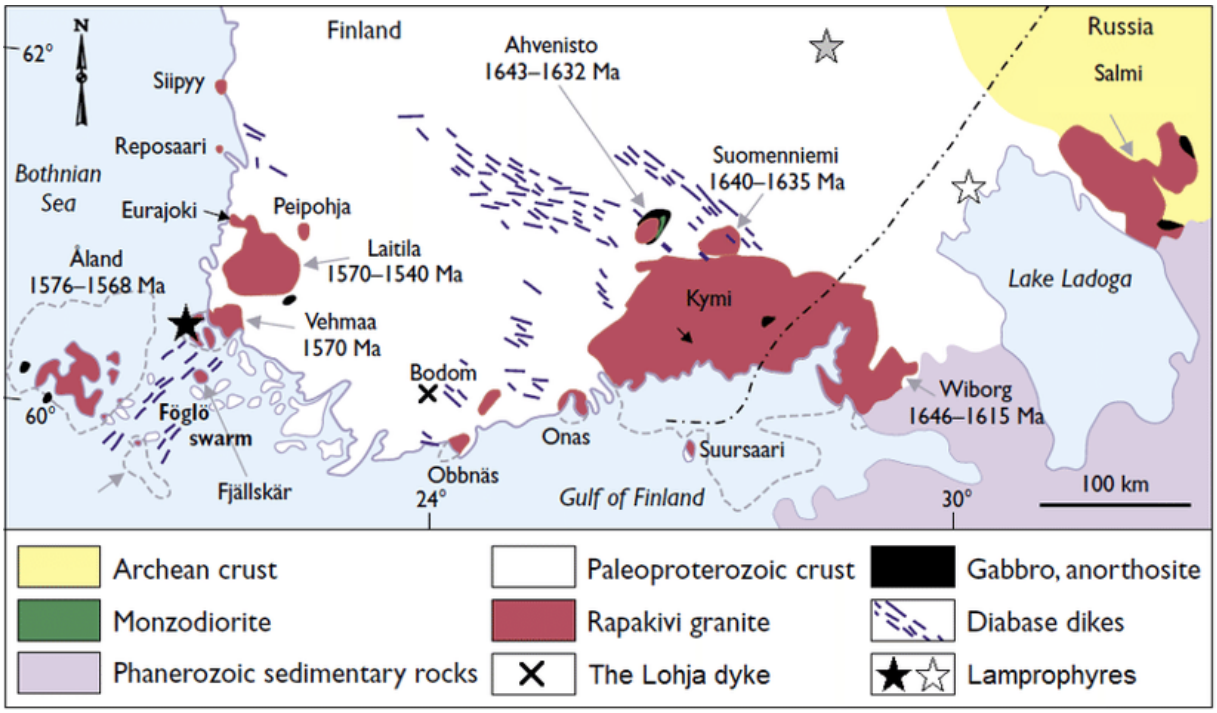

Figure 1. Geologic Map of the NW-SE trending rapakivi complexes in southern Finland and Russian Karelia. The studied Salmi batholith in the right corner. Source: Rämö and Haapala (2005)

zonation is also detectable in other rapakivi granites in the Fennoscandia shield (Sundblad, K. personal communication, 2020) Sundblad, K proposed that the batholith can be divided into five granite types depending on their degree of fractionation, the following order implies moving from south-east to north-west towards more evolved granites; Mustavaara, Repomäki, Nietjärvi, Mosautodor and Ristinoja.

The metal-fertility in the batholith is connected to the fractionation process (Haapala, 1995). Elevated In and Mo concentrations have been detected in the more evolved western parts of the batholith (K. Sundblad, personal communication, 2020). High Indium levels are only found in greisen veins in the most evolved granite (Ristinoja) in the batholith (K. Sundblad, personal communication, 2020).

The batholith is also connected to a large skarn deposit (Valkama et al., 2016a). At the western margin of the Salmi batholith lies an old mining area called Pitkäranta. The area contains 50 mines and where mined for Fe, Cu, Zn, Pb, Sn and Ag between 1810 and 1904. The Pitkäranta ores are formed in a skarn horizon created by metal-rich hydrothermal fluids thought to originate from the intruding Salmi Batholith (Valkama et al., 2016a).

The Pitkäranta minefield also contain elevated In grades. Indium was discovered 1910 in sphalerite at the ores by Wladimir Vernadsky (Valkama et al., 2016a). Today, Indium grades are estimated to be in the range of 100-500 ppm at Pitkäranta with sphalerite as the main carrier (Valkama et al., 2016a).

Methods

Data from six samples were analysed. All samples were collected from the Salmi rapakivi batholith by Krister Sundblad and are also petrographically described by Metso (2018). Four samples are from the inner part of the batholith: Mustavaara (KS1716, KS1710), Repomäki (KS1715), Nietjärvi (KS1718). Two samples represent granite types from the margin of the batholith: Mosautodor (KS1617) and Ristinoja (KS1626) (fig. 2 and table 1).

Table 1. Sample descriptions. Presented with increasing degree of fractionation downwards.

Sample	Rock Unit	Symbol
KS1716	Mustavaara	Black circle
KS1710	Mustavaara	Black square
KS1715	Repomäki	Red circle
KS1718	Nietjärvi	Green circle
KS1617	Mosautodor	Blue circle
KS1626	Ristinoja	Purple circle

Microscopy

A standardized petrographic microscope was used to preform thin section descriptions of the same samples. The thin sections were provided from the University of Turku.

Identification of minerals and structures followed standard routines.

Analytical method

The major- and trace element data was collected with an Agilent 8800 QQ ICP-MS connected to a New Wave 219 mm XXX laser ablation system. N_2O was used as reaction gas to enhance the separation between ^{115}In and ^{115}Sn successfully. The laser had a frequency of 10 Hz and the laser spots had a size of 60 µm. In total were 41 elements analysed (Appendix A and B). Internal standard NIST SRM 610 was used for all elements except for Fe, Mg, Ti and K were BCR-2G was used. Data reduction was made with Glitter™ software package.

LA-ICP-MS is an analytical technic where a laser beam is used on a sample to generate fine particles (Laser ablation) which becomes ionized and transported to a

mass spectrometer for rapid elemental and isotopic identification (fig. 3).

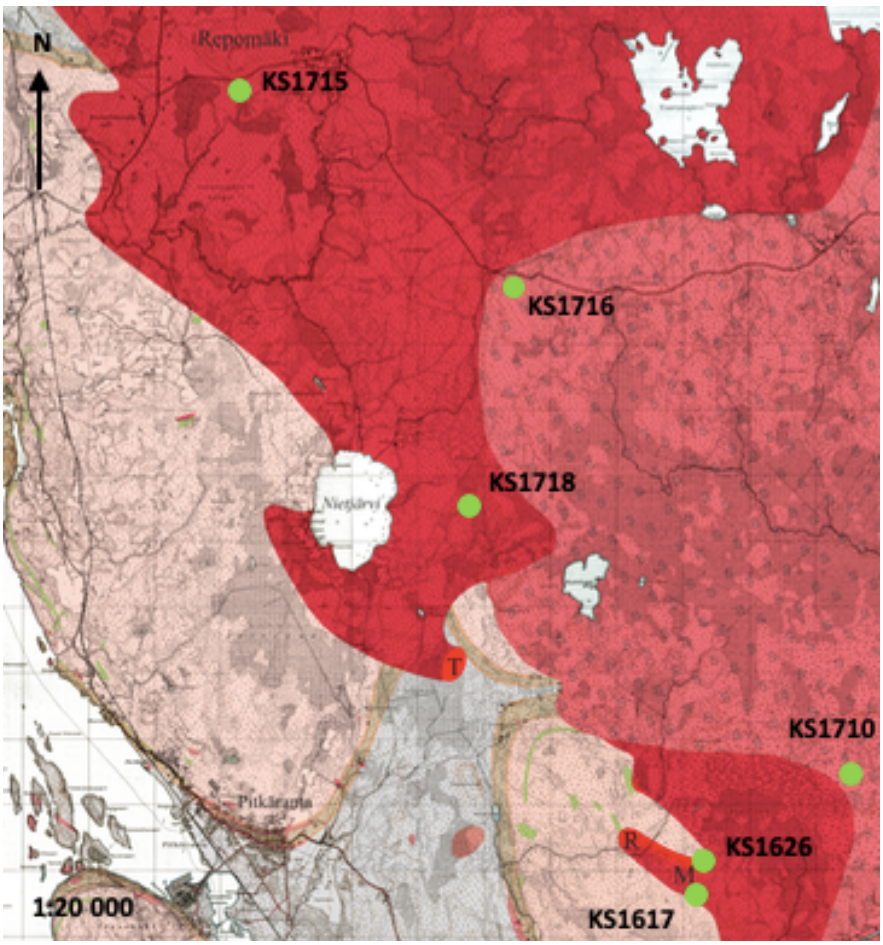

Figure 2. Geological map over the study area. The red colours are visualizing the salmi batholith. The map shows the western part of the batholith, Lake Ladoga is in the left corner. R = Ristinoja, M = Mosautodor. Modified from Sundblad et al. (in prep.)

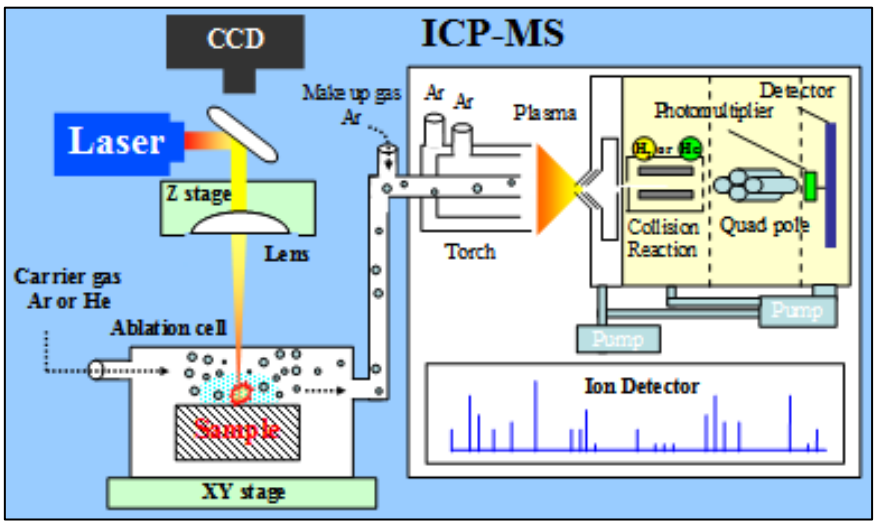

Figure 3. Schematic picture of LA-ICP-MS. Source: https://www.jfe-tec.co.jp/en/battery/analysis/material/la-icp-ms.html

A well understood difficulty with mass spectrometry is isotopic interference caused by isotopes of different species but with the same isotopic mass, isobars. This problem is solved by analysing isotopes without an isotopic interference. A problem arises when analysing indium because the metal lacks an isobaric interference-free isotope.

Indium has two isotopes ^{113}In and ^{115}In both in isobaric interference with ^{113}Cd and ^{115}Sn respectively. Indium measured in the thesis is ^{115}In due to its higher abundance (95,71 % of all In is ^{115}In) and the calculated concentrations for the element needs to be corrected for the interference with ^{115}Sn. The correction was done with BAM-S005 standard glass containing no Indium. All counts on mass 115 in the glass is ^{115}Sn. From the glass, a ratio was calculated between false identified In and correct identified Sn. The calculated ratio was then used for correcting measured In values.

Mica classification was performed with the major element data collected with LA-ICP-MS retained from the dark mica grains with promising results.

Mass balances were calculated for Rb, Ba, Zr, Hf, Nb, Ta, Zn, Sn, Mo, In, W, Li and Cu in samples KS1715 and KS1718 for plagioclase, K-feldspar and biotite. The samples were chosen because they contained measurements of all three phases. The calculations were made with measured element data in the phases and with unpublished bulk rock chemistry data from Krister Sundblad (appendix C, table 4).

Results

Petrography

The below section includes thin section descriptions from my work combined with mineral abundances and grains size observations from Metso (2018).

KS1710 – Mustavaara

The sample contain orthoclase (39 %), quartz (30 %), plagioclase (20 %) and biotite (10 %) as the main phases and chlorite, hornblende, zircon, fluorite, magnetite and apatite as accessory phases (1%).

The sample is coarse-grained with orthoclase as the largest crystals (5 – 13 mm), plagioclase (1,5 – 2,5 mm) and quartz (1,5 – 5 mm) occur in a semi-course grainsize (fig. 4A). Orthoclase is subhedral and contain perthite, the grains do also of enclose smaller quartz grains (fig.4B). Plagioclase grains are subhedral and exhibits albite and Carlsbad twining.

A vein cutting in the middle of the sample is visible both in the microscope and by the naked eye. It mainly contains quartz with plagioclase and orthoclase in a lower abundance. The largest biotite clusters found in the sample are also connected to the vein.

Biotite is subhedral with a grain size of 0,125 – 1,75 mm. They are mainly found in larger clusters (fig. 4D) in the vein, smaller assemblages are found in the other parts of the sample connected to orthoclase. The grains contain inclusions of zircon and apatite, fluorite is found in proximity. Parts of the biotite grains alters in a mild degree to chlorite. The hornblende found in the sample are always in connection with biotite where hornblende appears to alter to biotite (fig. 4C).

The alteration of the sample is evident. the minerals in the sample contain cracks filled with an Fe-rich fluid. Plagioclase and orthoclase alter to sericite in a similar degree.

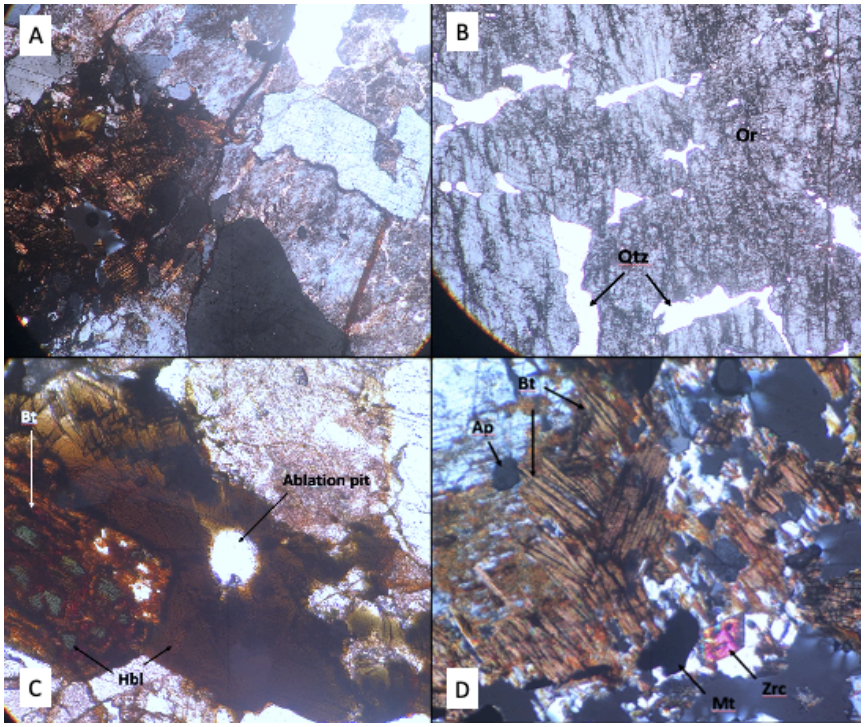

Figure 4. A, overview of sample KS1710 in cross-polarised light (5x magnification). B, quartz in sericite altered orthoclase (10x magnification). C, Ablation pit in hornblende. Hornblende alters to biotite. (10x magnification). D, Biotite. (10x magnification). Qtz = Quartz, Or = Orthoclase, Hbl = Hornblende, Bt = biotite, Ap = Apatite, Zrc = Zircon, Mt = Magnetite.

KS1716 – Mustavaara

The sample is generally coarse grained and dominated by orthoclase (43 %), quartz (40 %) and plagioclase (15 %) (fig. 5A). Orthoclase (2,5 – 12,5 mm) and quartz (1,25 – 5 mm) have the largest grainsizes, the grains are anhedral with sutured grain boundaries. Orthoclase contain perthite and show a poikilitic texture with plagioclase, biotite and smaller quartz grains. Plagioclase is smaller compared to orthoclase and quartz with a grain size between 0,5 – 2,5 mm. The plagioclase grains have anhedral to subhedral form and occur between grain boundaries and are enclosed by orthoclase.

A minor amount of small grained (0,25 – 4,25 mm) subhedral to euhedral biotite exists in the sample with an abundance of approximately 3% (fig. 5B). The grains show good cleavage and are often enclosed in orthoclase, but larger grains occur at grain boundaries in clusters. Inclusions of zircon, magnetite, apatite and monazite are seen in the biotite (fig. 5C). The degree of alteration to chlorite of the biotite grains are estimated to be very low at the rims to almost zero.

Accessory minerals found in the sample are zircon, magnetite, apatite, chlorite and monazite.

The summary of the alteration in the sample is very apparent. Cracks filled with magnetite and an Fe-rich fluid is visible both crossing grains and in grain boundaries (fig. 5D). Both orthoclase and plagioclase show alteration to sericite. The alteration in plagioclase are minor but orthoclase grains are heavily altered.

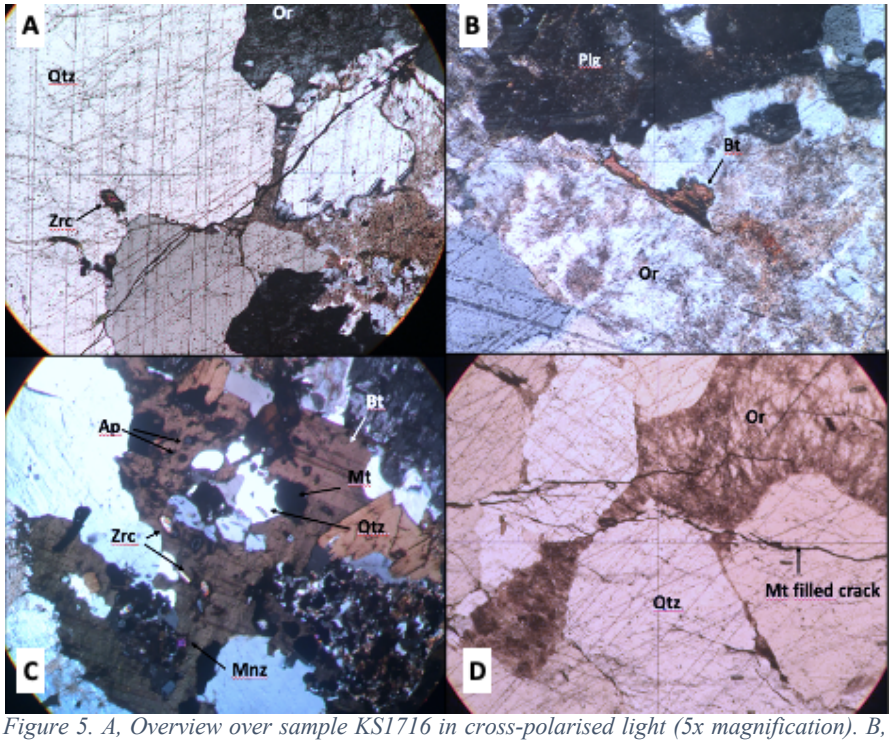

Figure 5. A, Overview over sample KS1716 in cross-polarised light (5x magnification). B, Biotite grain altered to chlorite at the edges (10x magnification). C, Biotite grain with several inclusions of apatite, monazite and zircon (10x magnification). D, Orthoclase altered to sericite. Magnetite filled crack crossing several grains. (5x magnification). Qtz = Quartz, Plg = Plagioclase, Or = Orthoclase, Bt = Biotite, Ap = Apatite, Zrc = Zircon, Mnz = Monazite, Mt = Magnetite.

KS1715 – Repomäki granite

The sample has a porphyritic texture with quartz as the main phenocrysts (2,5 – 3 mm) and with orthoclase (0,125 – 3 mm), plagioclase (0,125 – 0,75 mm), biotite (0,25 – 2,25 mm) and smaller quartz grains (0,25 –1 mm) making up the groundmass (fig. 6A). Phenocrysts consisting of orthoclase is also found to a lower extent. The sample consists of 32 % quartz, 30 % orthoclase, 29 % plagioclase and 9 % biotite. Chlorite, fluorite, zircon, muscovite and magnetite are found as accessory minerals in the sample.

The shape of the grains and degree of alteration is dependent on the mineral type. Quartz and orthoclase have anhedral to subhedral grains with sutured grain boundaries. Orthoclase show Carlsbad twinning and contain perthite, the mineral is altering to sericite. Plagioclase have subhedral to tabular euhedral crystals with albite twinning and have deformation twins in many grains. Alteration to sericite do also occur in plagioclase but to a lower extent compared to orthoclase.

The biotite grains in the sample are anhedral to euhedral. A small amount of biotite grains contains inclusions of zircon, monazite and magnetite. Where zircon or monazite are found, radiation halos are occasionally visible (fig. 6B). Fluorite with a tint of purple is also seen in the sample as inclusions in biotite or in proximity to the biotite grains (fig. 6C). The alteration of the biotite is more apparent in this sample compared to KS1716. The biotite alters to chlorite and muscovite both at the rims and within the biotite grains. The alteration to chlorite is distinct and, in some places, it has replaced large parts of the biotite grains (fig. 6D).

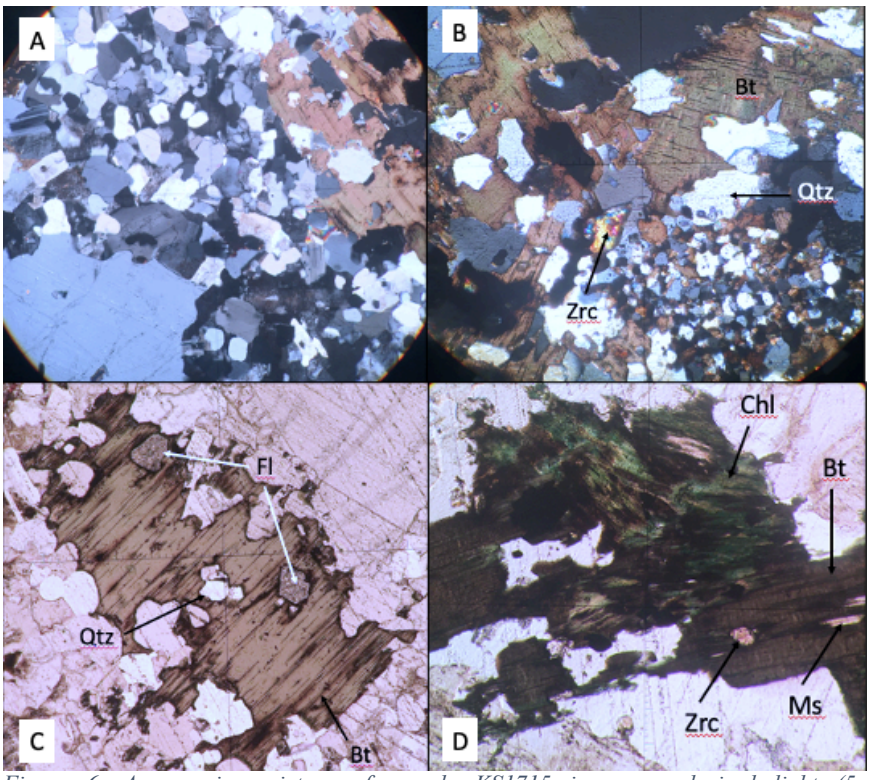

Figure 6. A, overview picture of sample KS1715 in cross-polarised light (5x magnification). B, Biotite grains with inclusions (10x magnification). C, Large biotite grain with fluorite inclusions (5x magnification). D, Chlorite altered biotite (5x magnification). Qtz = Quartz, Bt = Biotite, Ms = Muscovite, Chl = Chlorite, Fl = Fluorite, Zrc = Zircon,

KS1718 – Nietjärvi granite

The sample is weekly porphyritic with phenocrysts of orthoclase (1,25 – 5 mm) and quartz (2 – 3,75 mm), the sample have a medium grainsize in general (≈ 1,25 – 2,75 mm). The dominant mineral phases are Orthoclase (32,5 %), quartz (32,5 %), Plagioclase (30 %) and a minor amount of biotite (5 %). Accessory minerals found are chlorite, fluorite, zircon, muscovite, magnetite and titanite.

The overall texture in the sample are created by anhedral to subhedral crystals of quartz, orthoclase and plagioclase. Sutured grain boundaries are visible between quartz and feldspar in parts of the sample. The grain shape for quartz are anhedral, for orthoclase anhedral to subhedral and for plagioclase subhedral to tabular euhedral crystals. Plagioclase has developed an interlocking texture with feldspar and biotite (fig. 7A). Orthoclase shows Carlsbad twinning and perthite and plagioclase has albite twinning. Both orthoclase and plagioclase alter to sericite to a lesser extent. Several of the orthoclase grains exhibits a patchy texture with plagioclase (fig. 7B).

The biotite grains of the sample are anhedral to subhedral with grainsizes between 0,25 and 3 mm (fig. 7C). The grains have inclusions of zircon and purple tint fluorite, where radiation halos can be related to zircon inclusions. A variable degree of alteration to chlorite and muscovite is visible (fig. 7D). Larger grains are not altered to the same extent as smaller grains. Chlorite alteration is also more distinct than alteration to muscovite.

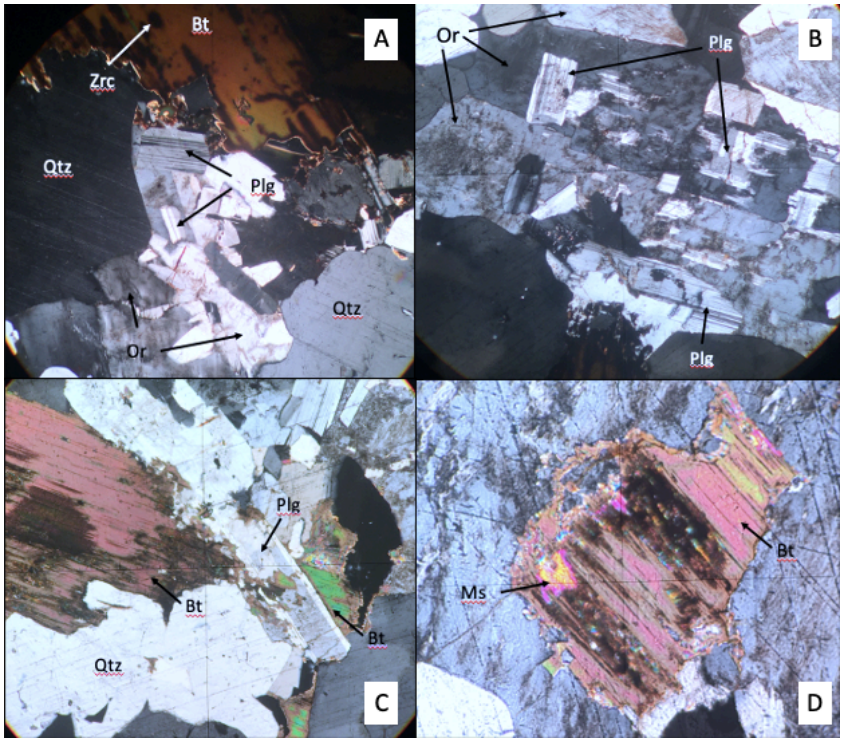

Figure 7. A, Overview in cross-polarised light of sample KS1718 (5x magnification). B, Patchy texture of orthoclase (5x magnification). C, Biotite overgrown with plagioclase (10x magnification). D, Biotite with alteration to muscovite (10x magnification). Qtz = Quartz, Plg = Plagioclase, Or = Orthoclase, Bt = Biotite, Ms = Muscovite, Zrc = Zircon.

KS1617 – Mosautodor granite

The sample have a medium grain size with a bimodal grain size. Quartz have the largest grain sizes between 0,25 – 2,25 mm and orthoclase- (0,25 – 1,25 mm), plagioclase- (0,25 – 1 mm) and biotite crystals (0,25 – 0,75 mm) have a smaller grain size. Subhedral to euhedral tabular plagioclase crystals and subhedral orthoclase forms an interlocking texture between the quartz crystals (fig. 8A). The abundance of the major minerals is 40 % quartz, 30 % orthoclase, 25 % plagioclase and 5 % biotite. Purple fluorite, chlorite, muscovite and magnetite are found as accessory phases in the sample.

The texture of the minerals is similar to the other described samples. Orthoclase often have Carlsbad twinning and perthite, showing exsolution texture between K-feldspar and plagioclase. Plagioclase show albite twinning and deformation twinning. Single smaller plagioclase grains are also often incorporated into the larger quartz crystals. The contact between plagioclase-quartz and orthoclase-quartz are often irregular. The sample also contain a vein filled with fluorite and quartz (fig. 8B)

Orthoclase and plagioclase show alteration textures. Both mineral phases are stained with an Fe-rich phase, this phase is more common in orthoclase compared to plagioclase. Orthoclase is also altered to sericite. Some plagioclase grains show a low grade of seritization.

The biotite grains in the sample is anhedral and to a large extent replaced by muscovite primarily (fig. 8D) and secondly, to a lower extent by chlorite (fig. 8C). Inclusions of magnetite and to some extent also fluorite is visible in the biotite grains, but the total amount of grains with inclusions are few. Fluorite is also found in proximity to biotite (fig. 8C, fig.

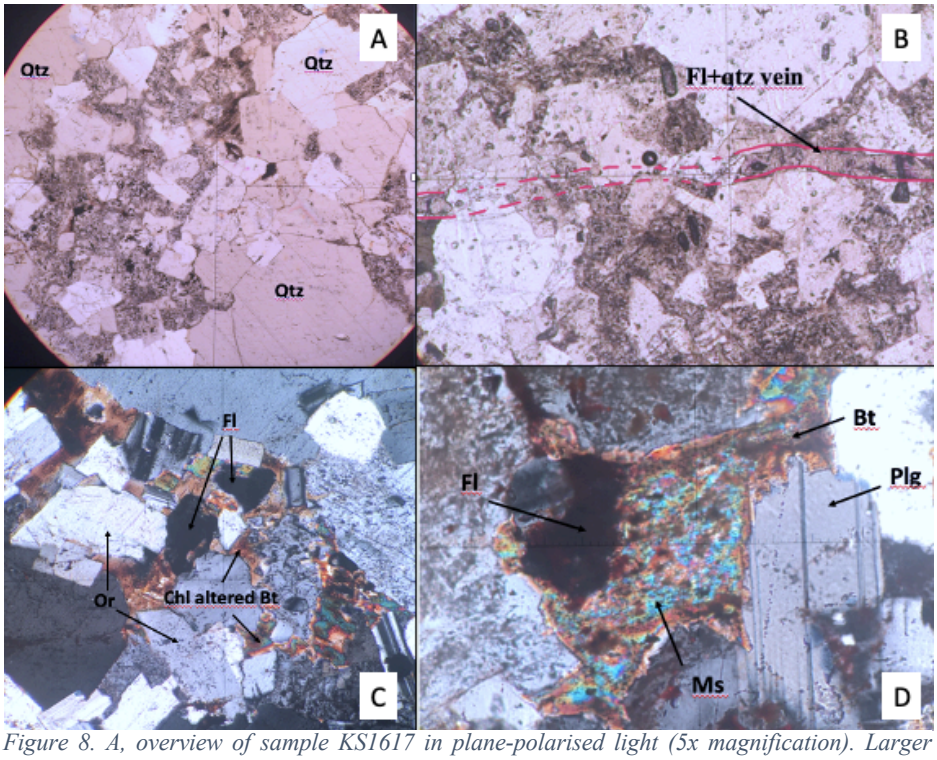

Figure 8. A, overview of sample KS1617 in plane-polarised light (5x magnification). Larger quartz crystals with a matrix of interlocking plagioclase and orthoclase (stained). B, Fluorite and quartz vein (5x magnification). C, Chlorite-altered biotite with fluorite (10x magnification). D, muscovite altered biotite (10x magnification). Qtz = Quartz, Plg = Plagioclase, Or = Orthoclase, Bt = Biotite, Ms = Muscovite, Chl = Chlorite, Fl = Fluorite

KS1626 – Ristinoja

Major mineral phases found in the sample are 35 % quartz, 30 % orthoclase, 30% plagioclase, 5 % biotite and 4 % microcline. Accessory mineral phases are chlorite, monazite, zircon and Fe-rich accumulations.

The most striking with the texture of the sample is the distinct irregular sutured grain boundaries between anhedral K-feldspar, plagioclase and quartz. The sample has a bimodal grain size distribution of medium sized grains. Quartz with grain sizes between 0,25 – 3 mm and orthoclase between 0,7 – 1,5 mm make up the semi-course grainsize of the sample; the smaller sized grains are microcline and plagioclase about 0,25 – 2 mm and biotite around 0,125 – 1 mm (fig. 9A).

The textures of the minerals in the sample are also prominent. Plagioclase and K-feldspar show undulose extinction and the formation of subgrains (fig. 9B). Plagioclase-grains do often contain deformation twinning. Microcline is identified in the sample with tartan twinning (fig. 9C). Orthoclase has no twinning and exhibits perthite in some parts of the sample. Quartz shows a weaker undulose extinction compared to K-feldspar and plagioclase.

The majority of the biotite in the sample are anhedral and undermined by plagioclase, K-feldspar and quartz (fig. 9D). The amount of inclusions in the grains are small, but in some parts of the sample radiation halos are visible in the biotite which indicates zircon inclusions. Smaller edges of individual biotite grains are also altered to chlorite.

The overall alteration of the sample is low. Orthoclase alters in mild degree to sericite and plagioclase is not altered to a notified degree. Some cracks filled with an Fe-rich fluid is visible within grains and along grain boundaries.

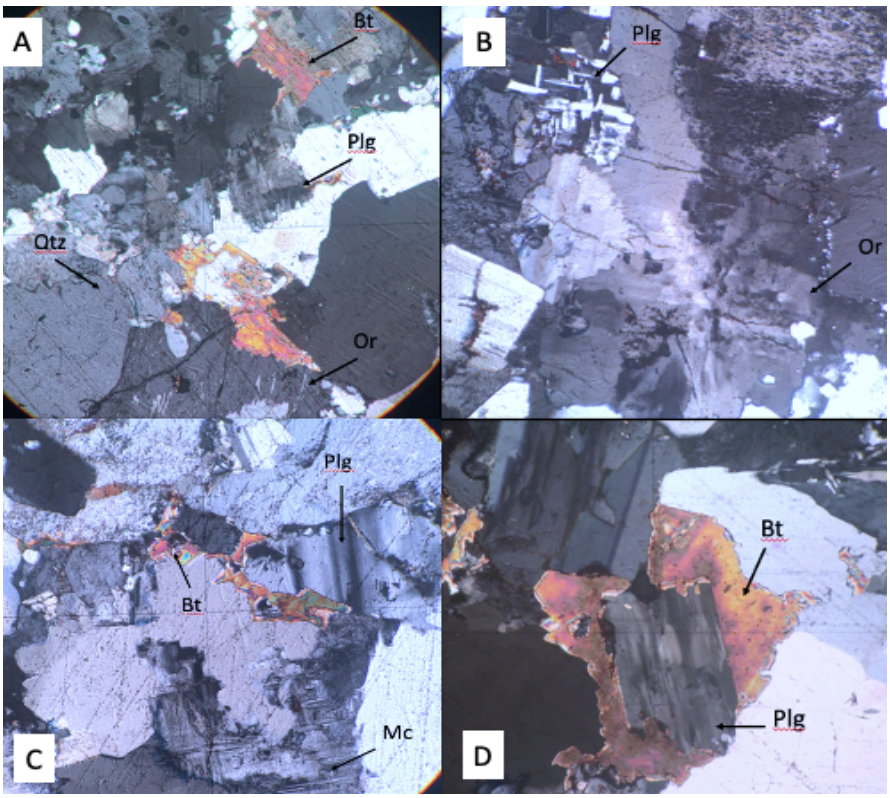

Figure 9. A, Overview of sample KS1626 in cross-polarized light. The picture shows several sutured grain boundaries between different phases. (5x magnification). B, Undulose extinction in orthoclase with sutured grain boundaries. (5x magnification). C, Microcline and plagioclase with twinning. (10x magnification). D, Biotite overgrown by plagioclase. (10x magnification). Qtz = Quartz, Plg = Plagioclase, Or = Orthoclase, Bt = Biotite.

Mica classification

Biotite from the same sample plots as clusters and Fe–Li rich biotite is found in all samples (fig. 10).

Biotite analysed in the samples from granite types within the batholith is composed of annite. The two samples from the margin of the batholith contain Li-rich siderophyllite.

The biotite grains display a fractionation trend from the batholith's interior towards it's margin (fig. 10). The biotite from the more evolved granite types contain an increased amount of Li. Similar trends, with increasing amount of Li in biotite from more evolved granites, is recognized in pegmatite fields in Norway by Rosing-Schow et al. (2018).

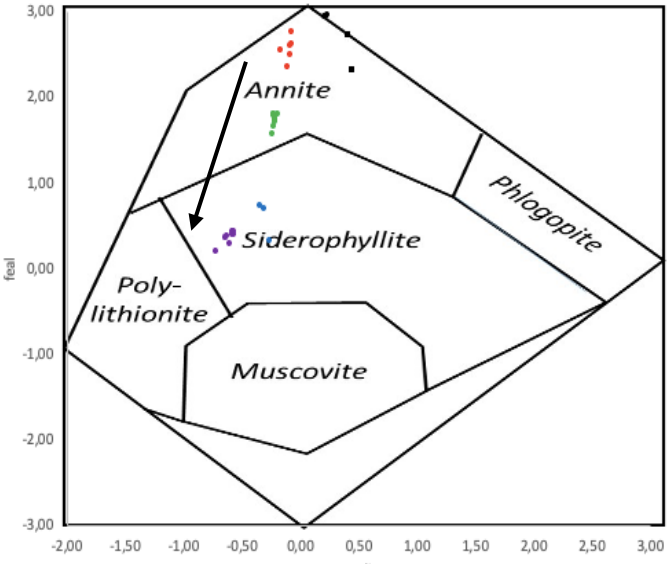

Figure 10. Mica classification. Black arrow showing fractionation trend. Modified from Tischendorf et al. (1997).

Major and trace elements

Biotite

The average composition* of biotite from each sample is presented in table 1 and 2. Major and trace element data for all measured biotite is presented in the appendix A and B. The average error for the measurements is 5 % for the major elements and 5-10 % for the trace elements.

Rubidium and barium concentrations show a negative correlation in the biotite grains from the different samples, Rb increases and Ba decreases (table 2). This reverse correlation give rise to an increase in the Rb/Ba ratio.

Rb/Ba plotted with Zr/Hf shows a week decreasing trend from Mustavaara, Repomäki to Nietjärvi and towards Mosautodor and Ristinoja (fig. 11).

A more evident decreasing trend is visible when Rb/Ba is plotted towards *feal* values (indication of fractionation in biotite) for the granite types (fig. 12).

The Nb/Ta ratio is also decreasing from the inner parts of the batholith towards the outer parts (fig. 13).

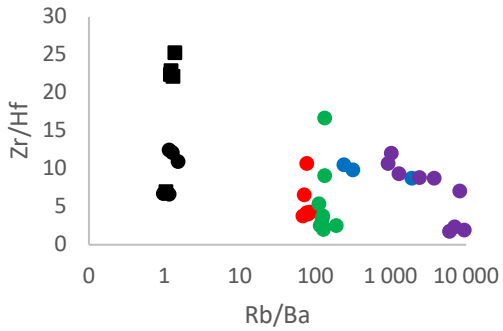

Figure 11. Zr/Hf values for analysed biotite plotted against biotite values for Rb/Ba, show a week deceasing trend.

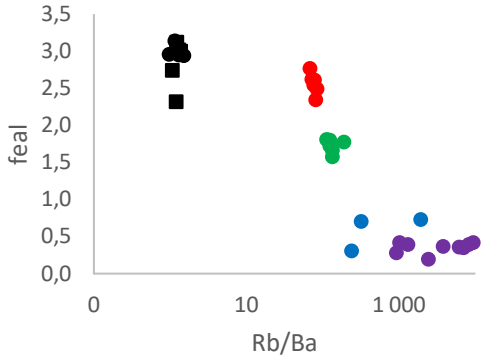

Figure 12. Feal values of biotite vs Rb/Ba ratio in biotite showing a decreasing trend.

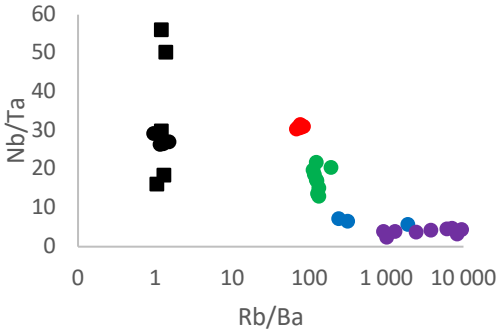

Figure 13. Nb/Ta ratio in biotite plotted towards Rb/Ba in biotite. The more evolved granites have a higher Nb/Ta ratio compared to the least evolved granites.

* Element data for sample KS1710 are presented with representative values from one measurement.

*Table 2. Average major oxide concentrations in wt% normalized to 94 % and stoichiometric formulas for biotite. *Element values for KS1710 are presented with a representative measurement. (Apfu = atom per formula unit*

Sample	KS1716	KS1710	KS1715	KS1718	KS1617	KS1626
Granite type	Mustavaara	Mustavaara	Repomäki	Nietjärvi	Mosautodor	Ristinoja
Mica	Annite	Annite	Annite	Annite	Siderophyllite	Siderophyllite
N	5	-	6	9	3	9
Meassurment	-	227	-	-	-	-
SiO_2 [wt%]	31,16	31,59	31,03	32,76	36,66	38,94
Al_2O_3	11,68	11,25	14,87	18,41	22,90	21,94
FeO	36,66	36,61	35,69	30,05	22,11	19,61
MgO	2,01	3,47	0,26	0,17	0,067	0,010
ZnO	0,18	0,11	0,17	0,17	0,10	0,15
CaO	0,09	0,31	0,003	0,004	0,007	0,001
Na_2O	0,074	0,24	0,065	0,12	0,11	0,18
K_2O	8,38	6,81	8,75	9,01	9,65	9,87
TiO_2	3,32	3,2	2,14	1,91	0,36	0,21
MnO	0,24	0,24	0,40	0,42	0,32	0,50
Rb_2O	0,11	0,076	0,21	0,24	0,49	0,57
Li_2O	0,10	0,094	0,40	0,74	1,24	2,02
Total [%]	94,00	94,00	94,00	94,00	94,00	94,00
Si [apfu]	2,684	2,692	2,650	2,685	2,802	2,961
^{IV}Al	1,316	1,308	1,350	1,315	1,198	1,039
Z	3,870	3,900	4,000	4,000	4,000	4,000
^{VI}Al	0	0	0,147	0,463	0,927	0,927
Fe^{2+}	2,641	2,609	2,549	2,059	1,476	1,247
Mg	0,258	0,441	0,033	0,021	0,010	0,001
Zn	0,011	0,007	0,011	0,010	0,004	0,009
Ti	0,215	0,205	0,138	0,118	0,024	0,012
Mn	0,017	0,017	0,029	0,029	0,017	0,032
Li	0,033	0,032	0,138	0,242	0,320	0,619
Y	3,176	3,311	3,045	2,942	2,778	2,847
K	0,921	0,741	0,953	0,942	0,949	0,957
Na	0,012	0,040	0,011	0,019	0,013	0,027
Ca	0,008	0,028	0,000	0,000	0,001	0,000
Rb	0,006	0,004	0,011	0,013	0,023	0,028
X	0,947	0,813	0,976	0,974	0,987	1,012
mgli	0,225	0,409	-0,105	-0,222	-0,310	-0,618
feal	3,003	3,009	2,569	1,743	0,590	0,364

*Table 3. Average trace element values for biotite in ppm. *Sample KS1710 is presented with a representative biotite measurement. (b.d = below detection limit)*

Sample	KS1716	KS1710	KS1715	KS1718	KS1617	KS1626
Granite type	Mustavaara	Mustavaara	Repomäki	Nietjärvi	Mosautodor	Ristinoja
Mica	Annite	Annite	Annite	Annite	Siderophyllite	Siderophyllite
N	5	-	6	9	3	9
Meassurment	-	227	-	-	-	-
Li [ppm]	445	437	1869	3418	5741	9402
B	11,75	12,79	6,39	8,36	24,36	14,47
P	285	151	149	113	156	126
Sc	22,32	48,47	25,10	15,28	25,78	20,98
V	54,39	110	3,38	1,17	0,23	0,057
Cr	28,64	61,08	0,29	0,12	0,23	0,20
Co	16,92	17,67	3,02	1,65	1,82	0,53
Ni	14,16	24,34	b.d	2,76	0,75	1,51
Cu	1,65	19,08	3,07	3,46	18,17	2,78
Zn	1416	884	1383	1342	782	1224
Ga	65,46	71,44	155	173	186	182
Ge	4,22	6,57	7,69	6,81	8,79	6,28
Rb	1049	695	1895	2224	4458	5209
Sr	1,04	5,34	0,17	0,20	0,78	0,11
Y	16,51	54,93	1,13	4,27	102	5,09
Zr	1,42	26,15	2,44	5,95	177	23,15
Nb	341	179	543	745	560	389
Mo	1,51	1,69	7,55	2,50	1,20	0,79
In	0,28	0,37	1,06	0,42	0,21	0,38
Sn	14,43	17,85	99,41	178	123	349
Sb	0,03	b.d	0,10	0,20	0,19	0,22
Cs	39,77	42,10	31,58	47,35	119	342
Ba	880	504	24,87	17,23	9,21	2,35
Ce	6,15	716	0,62	4,19	14,90	5,51
Hf	0,15	1,03	0,41	0,75	17,28	2,42
Ta	12,33	3,57	38,04	44,39	103	96,60
W	0,33	2,35	1,73	2,23	22,38	18,81
Tl	6,08	4,42	11,33	12,92	16,28	18,39
Pb	5,87	83,85	4,49	8,45	10,01	9,64
Bi	0,031	1,29	0,034	0,020	0,083	0,069

Elements seen to decrease from Mustavaara to Ristinoja are V, Cr, Co, Ni and Ti. Elements that show an increase in concentrations in the biotite grains from Mustavaara to Ristinoja are Ga, Cs, Ta, Tl. Lithium show a strong increasing trend within the micas from Mustavaara to Ristinoja (fig. 14A). Low values of W are recognized in the biotite from Mustavaara, Repomäki and Nietjärvi, but the metal is enriched in Mosautodor and Ristinoja (fig. 14B). No large variation in concentrations between biotite from different granites are seen for Pb, Ge, Sc.

Other measured elements in the biotite grains show more complex trends. Molybdenum and indium behave similar with a wider spread of concentrations in the Mustavaara samples and with an enrichment spike in the sample from Repomäki (fig. 14 C and D). In Nietjärvi, Mosautodor and Ristinoja the concentrations decrease for both elements.

Metals associated with indium, as described in the introduction such as Cu, Zn and Sn, are not showing the same pattern as In.

Tin show a strong increasing decoupled trend in the samples from Mustavaara to Ristinoja, the decoupling is caused by the sample from Mosautodor which contain low Sn ppm values compared to the other granites (fig. 15A). Zink does not show a trend because the variations between the granite types are small (fig. 15B). Copper is similar to Zn but with elevated ppm values in two of the analysed biotite within the sample from Mosautodor. The outliers can be explained with heterogeneities within a single grain, such as inclusions of sulphides (fig. 15C)

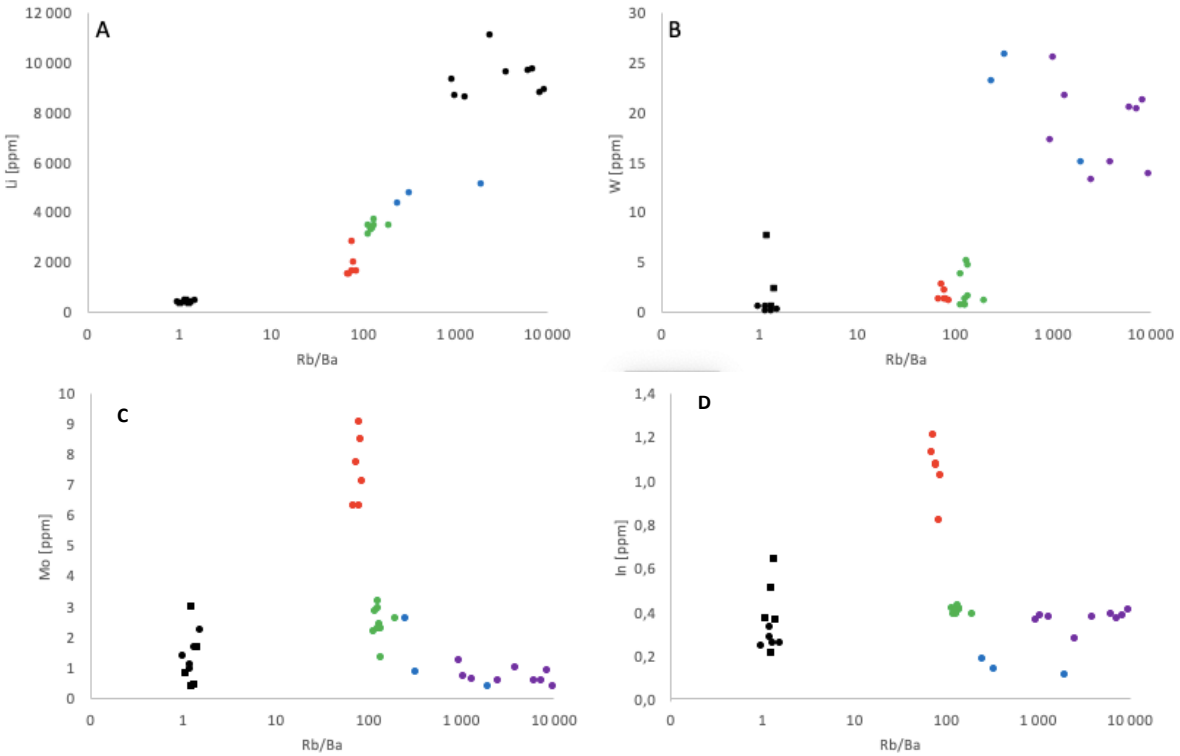

Figure 14.Trace element variations in biotite plotted against Rb/Ba ratio in biotite. A, Li variations biotite with a clear increasing trend. B, W in biotite with higher values in the more fractionated granite types. C, Mo concentrations in biotite only showing enrichment in the sample from Repomäki. D, Variations of In between the different granite types within biotite.

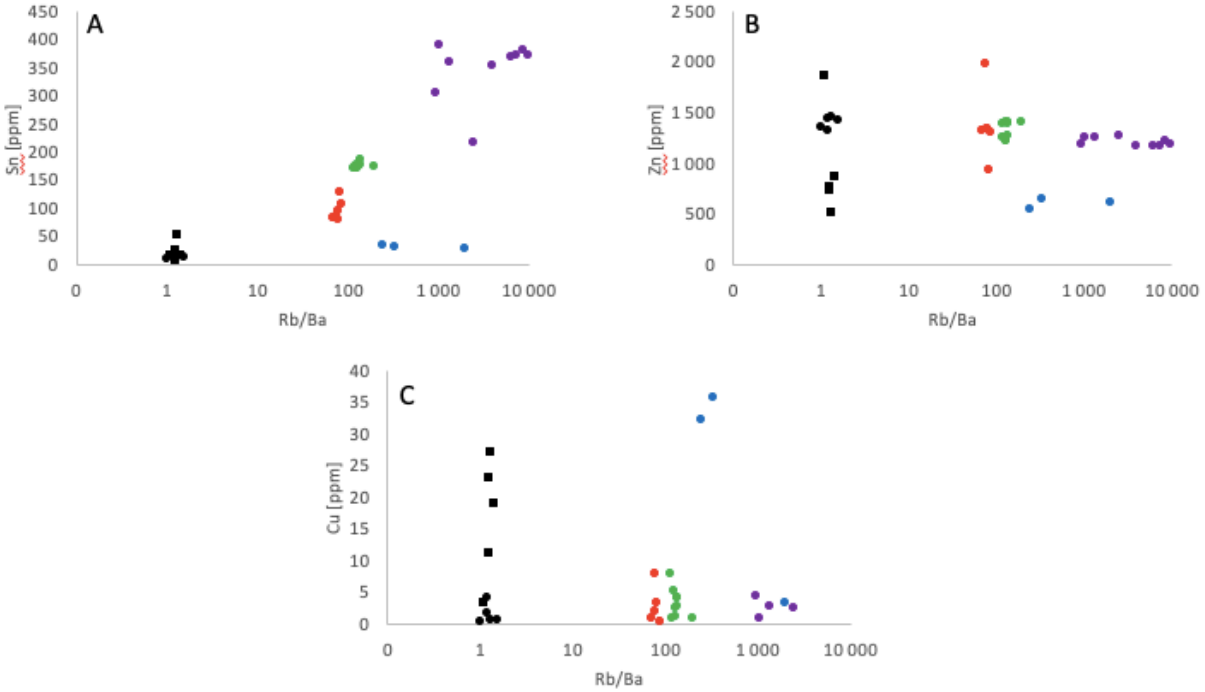

Figure 15. Metal variations in biotite with Rb/Ba in biotite as differentiation index A, Sn variations in biotite showing a strong increase with higher degree of fractionation. B, Zn in biotite displaying no large variations between the granite types. C, Cu grade

Indium in Amphibole, Plagioclase, K-feldspar and Quartz

The average In concentrations are low to very low in quartz, plagioclase and K-feldspar (fig. 16). The concentration of In in biotite is significantly higher. Amphibole show higher In concentrations compared to biotite (fig. 17). This patterns is also recognized by Knighton (2015).

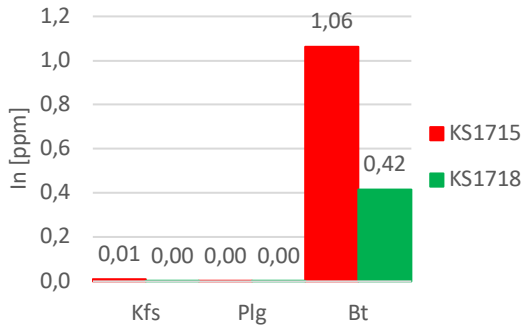

Figure 16. Comparison of In grades between analysed phases in sample KS1715 and KS1718.

Mass balance calculations

Mass balances are calculated for Rb, Ba, Hf, Zr, Nb, Ta, Li, Zn, Sn, Mo, In, W and Cu between plagioclase, K-feldspar and biotite in two out of six samples (fig. 18). It is visible that Ba grades in the whole rock are mainly controlled by K-feldspar. The controlling hosts for Rb and Cu seem to be equally distributed between plagioclase, K-feldspar and biotite. In the samples the measured phases are not thought to control the values for Zr and Hf in the whole rock. Zr is more likely to be controlled by zircon. A difference between the samples are the phases thought to control Mo concentrations in the rock. In sample KS1715 Mo are thought to mainly be controlled by phases not analysed. Sample

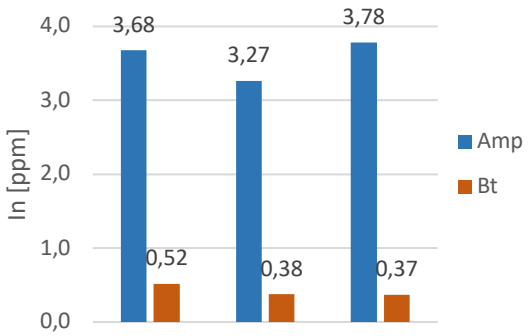

Figure 17. Comparison of In grades between amphibole and biotite in sample KS1710.

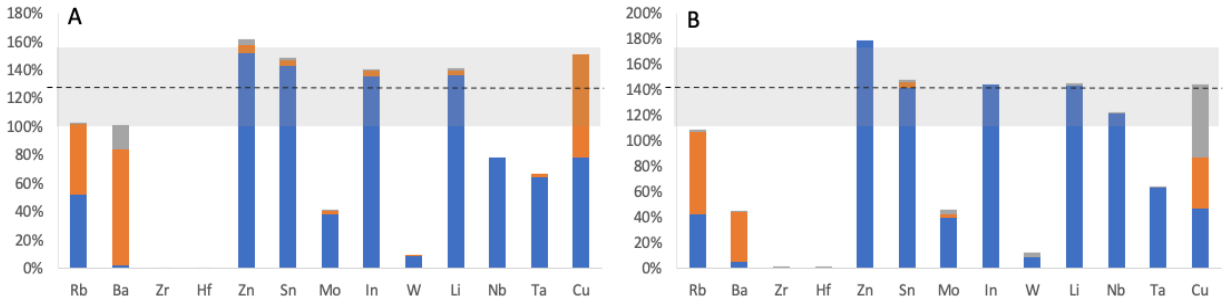

Figure 18. Mass balance calculations for A, sample KS1715 and B, sample KS1718. Grey = Plagioclase, Orange = K-feldspar, Blue = Biotite. Grey area = plus/minus mass balance achieved with minerals considered.

KS1718 is different, where Mo in the whole rock is showed to be mainly controlled by biotite. The calculations are also indicating that Zn, Sn, In and Li concentrations are mainly controlled by biotite.

Values for In, Li and Cu in the bulk rock for sample KS1715 and In, Li, Cu and Mo grades in the bulk rock for sample KS1718 should be viewed with caution. The element values mentioned are calculated because measured values were below detection limit.

Discussion

Petrography

The samples from the inner part of the batholith (Mustavaara, Repomäki and Nietjärvi) all have a coarser grain size compared to the samples from the outer parts (Mosautodor and Ristinoja). The larger crystals in the three samples from the inner part of the batholith are orthoclase and quartz and they display similar textures and degree of alteration to sericite and chlorite. The biotite grains in the samples from Mustavaara, Repomäki and Nietjärvi are also similar with a more subhedral to euhedral shape and not clearly undermined by the other minerals.

The granite types from the batholiths margin, Mosautodor and Ristinoja, also show similar textures. Both samples have a bimodal grain size with quartz as larger crystals. Plagioclase and orthoclase are forming an interlocking texture in between the quartz crystals and sutured grain boundaries are seen in the whole samples to a large extent. The biotite grains within the samples are also similar with an anhedral crystal shape undermined by quartz, plagioclase and orthoclase. Muscovite alteration in the biotite is more prominent compared to the chlorite alteration. The degree of alteration to sericite in both these samples are also lower compared to the other three samples (Mustavaara, Repomäki and Nietjärvi).

A general grain size reduction is visible between the granite types in the following order: Mustavaara, Repomäki, Nietjärvi, Mosautodor to Ristinoja. This is consistent with the observation reported by Metso (2018). The general grouping of the granite types with respect to textures with Mustavaara-Repomäki-Nietjärvi and Mosautodor-Ristinoja is also recognized by Metso (2018).

In general, all the samples show an igneous fabric overprinted by metamorphic and hydrothermal textures. The alteration to sericite in orthoclase and to a smaller extent in plagioclase grains, mainly in Mustavaara and Repomäki, is indicative for a Phyllic-alteration. It is a hydrothermal alteration which includes replacement of feldspar with sericite (fine grained mica) through hydrolysis and can occur over a range of temperatures (Robb, 2005). Furthermore, the chlorite and muscovite alteration of biotite is also indicative for a hydrothermal alteration process. In the samples from Repomäki, Nietjärvi and Mosautodor fluorite is found as an accessory phase and fluorine might be interpreted to have been transported with the hydrothermal fluids

and allowing for fluorite to crystallize in the samples. The hydrothermal alteration is more prominent in the samples representing granite types from the inner parts of the batholith but do exist in all samples. In Mosautodor and Ristinoja (as well as Nietjärvi to a lower extent) micro textures indicating recrystallization is more common. Sutured grain boundaries, the formation of subgrains and deformation twinning indicate deformation of the samples at relatively high temperatures (500 °C) (Winter, 2014).

The degree of recrystallization textures in the samples increases going from Mustavaara, Repomäki via Nietjärvi, Mosautodor to Ristinoja.

Trace elements in biotite

The decrease of V, Cr, Co, Ni and Ti in the biotite may be caused by their compatible behaviour. These elements will be incorporated into early crystallizing phases and will not become enriched in the biotite crystallizing in more evolved granite types. Ga, Cs, Ta, Tl, Sn and Li are seen to increase in the biotite grains due to their incompatible nature. They get enriched because they are more preferentially incorporated into the melt. Zn, Cu, Ge, Sc and Pb show no trend in the samples and are therefore interpreted to not be affected by the fractionation process in the biotite.

Rb/Ba

The increasing Rb/Ba ratio indicate on a fractionation of biotite. Rubidium and barium are Large Ion Lithophile (LIL) elements. Due to their large ionic radii they are classified as incompatible elements, but the low charge makes the elements easily mobilized by hydrous fluids (Winter, 2014). Rubidium has a monovalent state and is more incompatible in comparison to the divalent Barium ion. Rubidium values are increasing from Mustavaara to Ristinoja and the opposite pattern is seen for Ba caused by a fractionating granitic system.

The fractionation pattern between the granite types within the biotite are clearly visible when plotting Rb/Ba against *feal* values.

Controlling Rb/Ba values

There is a positive correlation between measured Rb/Ba values in the biotite and Rb/Ba values calculated from the bulk rock (fig. 20). The trend is offset with higher Rb/Ba values in the biotite crystals and thus not giving a 1:1 relationship to the values from the bulk rock. This suggests that Rb and/or Ba concentrations in the bulk rock is not only controlled by biotite. The mass balance calculation is suggesting that K-feldspar is a dominant phase controlling the Ba concentrations and causing the offset in Rb/Ba ratios between the bulk rock and biotite.

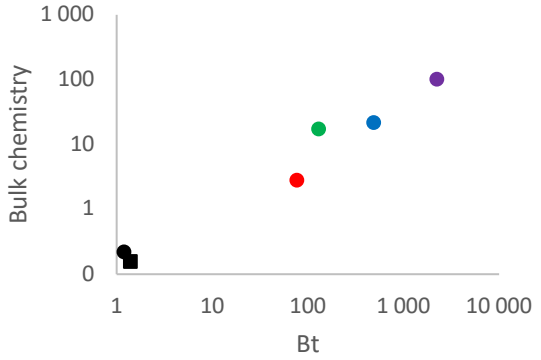

Figure 19. Plot with average Rb/Ba values for measured biotite compared with unpublished Rb/Ba values for the bulk rock from Krister Sundblad.

Despite the offset visible between the ratios in the biotite crystals and the bulk rock, the change in Rb/Ba in the bulk rock chemistry is still recognized in the biotite crystals. Furthermore, biotite may therefore be used as an indicator mineral for fractionation processes in the bulk rock.

Zr/Hf

A week fractionation between Zr/Hf are also evident in the biotite. The fractionation trend is also recognized more clearly in the whole rock chemistry (fig. 19) (K. Sundblad, unpublished data).

The lack of a clear trend in the biotite can be explained by lower variations of the

Zr/Hf ratio. The low variations in the ratio can be caused by biotite containing low concentrations of Zr and thus be affected by analytic uncertainties. It can also be explained with biotite not thought to control Zr and Hf concentrations in the bulk rock, which the mass balance calculations are indicating. Zircon is thought to more likely be controlling the Zr concentrations in the bulk rock and thus give low Zr values in biotite.

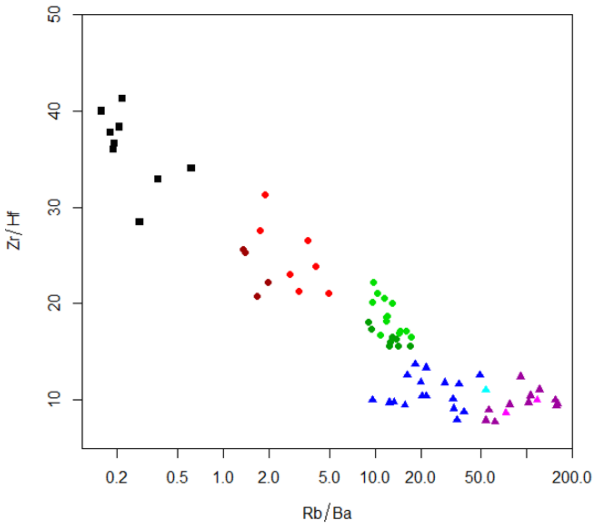

Figure 20. Zr/Hf ratio plotted against Rb/Ba values from whole rock dataset. The plot displays a decreasing trend showing an increase in degree of fractionation towards Mosautodor and Ristinoja. Black = Mustavaara, Red = Repomäki, Green = Nietjärvi, Blue = Mosautodor, Purple = Ristinoja. Source: Unpublished data from Krister Sundblad.

Nb/Ta

Niobium and tantalum has often been referred to as chemical identical twins because of their similar behaviour in magmatic fractionation processes (Green, 1995). Despite this, fractionation of these elements can be caused by metasomatism where Ta is more favoured in the fluid-phase (Green, 1995).

The Nb/Ta ratio is decreasing with increasing fractionation in the granite types, Mosautodor and Ristinoja contain the lowest values around 6 and 4 respectively. Generally, A-type granites are recognized to have low Nb/Ta values caused by the involvement of fluids in the fractionation process (Green, 1995). The activity of fluids in the Salmi batholith is evident in the microstructures described from the thin sections and thus fluids may be causing the fractionation of Nb and Ta.

Lithium

A clear increasing trend for Li is seen with an increasing degree of fractionation in the biotite. Within more matured biotite, K^+ is seen to be replaced in a larger extent by Li^+. The described trend is also recognized in pegmatitic systems by Rosing-Schow et al. (2018).

Tungsten

The fractionation process in biotite are affecting the behaviour for tungsten. The least evolved granites have lower grades of W compared to the more evolved granite types.

The lower W concentrations in the granites from the inner part for the batholith can be explained with other phases incorporating the metal. The element is most likely to be hosted by other tungstate phases such as wolframite, but this cannot be confirmed since these phases is not identified in the samples.

Molybdenum

The behaviour of Mo is not seen to be affected by the fractionation process in biotite. The only sample having higher grades of Mo is Repomäki, the other samples do all contain similar concentrations of the metal. The high Mo concentrations from Repomäki can be connected to higher Mo grades in the whole rock and the identification of molybdenite in one of the samples (Unpublished data, Sundblad, K.).

The lower Mo concentrations could also be explained by other phases incorporating the metal. Because the higher concentration of Mo in the host rock from Repomäki is mirrored in the biotite from the same granite type this explanation is not likely.

The biotite grains are not indicating on a Mo enrichment in the most evolved granite types. The elevated Mo grades in the

greisen veins connected to the granite types are not reflected in the biotite.

Tin

Tin is evidently getting enriched through the fractionation process in the biotite. The biotite in Ristinoja contain up to 390 ppm Sn and Nietjärvi have concentrations up to 180 ppm. The Sn pattern for biotite is also recognized in unpublished bulk chemistry data for the whole rock from Krister Sundblad, but the grades in biotite is generally higher and show larger variations. The higher Sn grades in biotite may be explained by that biotite is controlling the tin concentrations in the whole rock.

One exception from the increasing trend is the sample from Mosautodor, were the Sn concentrations are deviating and are only around 32 ppm. The depletion of Sn is also recognized in the bulk rock data for the same granite type and can therefore be explained by generally lower Sn grades in the whole granite.

Sample KS1626 representing Ristinoja contain the highest Sn values with an average of 348 ppm. Greisen veins found adjacent to the sample location is also reported to have very high Sn grades with up to 0,42 % (personal communication, Sundblad, K.) The correlation between these high values may indicate a connection between the greisen veins and Ristinoja and additionally that biotite is able to record anomalous high Sn concentrations in the granitic system.

The strong increase of Sn towards the batholith's margin may indicate that the Salmi batholith is the source for the Sn enrichments at Pitkäranta. The high concentrations recorded in the biotite makes it possible for exsolving fluids originating from the batholith to contain elevated Sn grades.

Zinc

The fractionation process is not though to affect the Zn grades in biotite.

The lack of an Zn enrichment in the more evolved granites is indicative on that the batholith can't have exsolved an fluid enriched in Zn. The Zn in the Pitkäranta ores may not have originated from the Salmi batholith.

Copper

The measured Cu in the biotite is not affected by the fractionation process. Because of the low Cu concentrations in the biotite, exsolving fluids from the batholith is not thought to have been enriched in Cu. The Cu-deposits at Pitkäranta is more likely to have been enriched by Cu originated from an external lithology.

Indium distribution between analysed phases

The partition coefficient for indium in amphibole is evidently higher compared to biotite. This results is in agreement with with the experimental work by Gion et al. (2018) implying a higher D_{In} in amphibole compared to biotite.

Indium mineralizations

Indium is not evidently affected by the fractionation process in the biotite and thus show no enrichment. All samples except KS1715 (up to 1,20 ppm) contain similar In values around 0,2 – 0,4 ppm. In the Salmi batholith, indium is thought to behave more as an moderately compatible element in contrast to what Schwarz-Schampera and Herzig (2002) described.

A contrasting argument explaining the lack of In-enrichment is another phase taking up the available In in the melt. As indium is associated with Zn, Cu, Sn and likely to substitute for these elements in sulphide minerals (Schwarz-Schampera and Herzig, 2002), the low In values in biotite can imply crystallization of sphalerite, chalcopyrite or stannite. This argument ca be dismissed by the low Zn, Cu and Sn grades in the bulk rock (appendix C, table 4) (K. Sundblad, personal communication) and the mass balance calculations for In.

The low abundance of Zn, Cu and Sn in the granites is not enough for crystallizing

their own phases and affect the In concentration in biotite. The mass balance calculations are showing that biotite is controlling In concentrations in the whole rock and the In grades are therefore not likely to be affected by other present phases.

The missing indium enrichments in the more evolved granites are indicative of a low probability for an In-rich fluid to exsolve from the batholith. The In in Pitkäranta is more likely to originate from an external source.

Additionally, due to the lack of an In enrichment in biotite the model proposed by Gion et al. (2019) for the creation of indium deposits related to granitic systems may not be applicable on this system. The amount of amphibole in the samples is very low to almost non and should not affect the possibility for indium enrichment to take place. Also, Fe-rich biotite is the main ferromagnesian phase. Because of this according to the model, an indium enrichment should be visible in the batholith. The result is not in agreement with the above and it is not evident that the biotite has enhanced an enrichment of indium. Accordingly, this model may not be appropriate to describe the granitic system in the Salmi batholith.

Molybdenum and Indium

Indium and molybdenum behave very similar in the system with low values in all samples except KS1715 from Repomäki. It was expected for In to behave like other moderately incompatible elements such as W, Sn and Li.

Neither Mo nor In is seem to be evidently effected by the fractionation process in the biotite and thus both elements may more accurately described as moderately compatible elements in this system. These results are in disagreement with Simons et al. (2017) showing that In behaves similar to moderately incompatible elements such as W, Nb and Ta.

Biotite as an exploration vector

The biotite grains show no elevated In values and no increase in indium with increasing fractionation. Because of this no indication of local In-rich deposits can be interpreted from the biotite grains in this system.

In addition to this, the concentrations of Sn are strongly showing an increasing trend in the biotite grains which is also visible in the whole rock and can thus indicate on possible local enrichments within the batholith.

Conclusions

- The samples from Mustavaara, Repomäki and Nietjärvi contain similar textures with a coarse grain size and a porphyritic character. The larger crystals in the samples are orthoclase and quartz. The biotite is similar in all four samples with a subhedral to euhedral shape. The alteration in the samples are widespread and biotite alters mainly to chlorite. Microstructures described in the thin sections is suggested to indicate on hydrothermal alteration of the samples.

- The samples from Mosautodor and Ristinoja have a medium grain size where quartz can be seen as larger crystals. The samples contain more pronounced recrystallization textures and the biotite are anhedral and undermined by quartz, K-feldspar and plagioclase. The alteration to muscovite in biotite is more common compared to chlorite alteration. The large amount of recrystallization textures is indicating that the samples have undergone metamorphism under elevated temperatures.

- A decrease in grain size is identified from Mustavaara–Repomäki–Nietjärvi to Mosautodor–Ristinoja.

- Moving from Mustavaara–Repomäki–Nietjärvi to Mosautodor–Ristinoja an increasing degree of fractionation is identified in the biotite.

- The amount of Li and ^{IV}Al incorporation is increasing within biotite from more evolved granites.

- The major indium hosts in the Salmi batholith are the ferromagnesian phases, biotite and amphibole. When amphibole is present the In grade in the mineral is higher compared to biotite. When biotite is the only ferromagnesian phase the mineral is controlling the In concentrations in the bulk rock. It is not evident that In is affected by the fractionation process within the biotite form the Salmi batholith.

- In the Salmi batholith, it is not suitable to use indium in biotite as an exploration vector for finding local In-rich metal deposits but, the usage of Sn in biotite should be considered further. Tin are increasing within the biotite with the evolving magmatic system and with a general increase of the Sn in the whole rock.

Acknowledges

I would like to thank my advisor Dr. Thomas Zack for presenting the work to me and also making it possible to finish despite the pandemic crisis. I also wish to express my gratitude towards Krister Sundblad for providing the samples and helping me with guidance.

References

Amelin, Y.V., Larin, A.M., Tucker, R.D., 1997. Chronology of multiphase emplacement of the Salmi rapakivi granite-anorthosite complex, Baltic Shield; implications for magmatic evolution. Contributions to Mineralogy and Petrology, 127(4): 353-368.

Ballouard, C. et al., 2020. Magmatic-hydrothermal evolution of rare metal pegmatites from the Mesoproterozoic Orange River pegmatite belt (Namaqualand, South Africa). Ore Geology Reviews, 116.

Broman, C., Sundblad, K., Valkama, M., Villar, A., 2018. Deposition Conditions for the Indium-Bearing Polymetallic Quartz Veins at Sarvalaxviken, south-eastern Finland. Mineralogical Magazine, 82: 43-59.

Calzia, J.P., Rämö, O.T., 2005. Miocene rapakivi granites in the southern Death Valley region, California, USA. Earth Science Reviews, 73(1): 221-243.

Cook, N. et al., 2011. Indium mineralisation in A-type granites in southeastern Finland: Insights into mineralogy and partitioning between coexisting minerals. Chemical Geology.

European Commission, 2014. Report on Critical Raw Materials for the EU, European Comisson, , European Commisson, .

Gion, A.M., Piccoli, P.M., Candela, P.A., 2018. Partitioning of indium between ferromagnesian minerals and a silicate melt. Chemical Geology, 500: 30-45.

Gion, A.M., Piccoli, P.M., Candela, P.A., 2019. Constraints on the formation of granite-related indium deposits. Economic Geology and the Bulletin of the Society of Economic Geologists, 114(5): 993-1003.

Green, T., 1995. Significance of Nb/Ta as an indicator of geochemical processes in the crust-mantle system. Chemical Geology(120): 347-359

.

Haapala, I., 1995. Metallogeny of the Rapakivi granites. Mineralogy and Petrology, 54(3): 149-160.

Haapala, I., Rämö, O.T., 1999. Rapakivi granites and related rocks: an introduction. Precambrian Research, 95(1): 1-7.

Hazen, R.M., Wones, D.R., 1972. The effect of cation substitutions on the physical properties of trioctahedral micas. American Mineralogist, 57(1-2): 103-129.

Knighton, S., 2015. Indium Distriution among Select Granitic Minerals.

Larin, A., 2009. Rapakivi granites in the geological history of the earth. Part 1, magmatic associations with rapakivi granites: Age,

geochemistry, and tectonic setting. Stratigraphy and Geological Correlation, 17(3): 235-258.

Metso, S., 2018. Petrography of seven Granite Types in the the Salmi Rapakivi Batholith, Russian Karelia BSc Thesis, University of Turku.

Nesse, W.D., 2012. Introduction to Mineralogy. Oxford University Press, New York.

Robb, L.J., 2005. Introduction to Ore-forming Processes. Blackwell Publishing.

Rosing-Schow, N., Mûller, A., Friis, H., 2018. A Comparison of the Mica Geochemistry of the Pegmatite Fields in Southern Norway. The Canadian Mineralogist, 56: 463-488.

Rämö, O.T., Haapala, I., 2005. Rapakivi Granites. In: Lethinen, M., Nurmi, P.A., Rämö, O.T. (Editors), Precambrian Geology of Finland – Key to the Evolution of the Fennoscandian Shield. Elsevier Science, pp. 533-562.

Schwarz-Schampera, U., Herzig, P.M., 2002. Indium: Geology, Mineralogy and Economics. Springer Berlin Heidelberg, pp. 1-23.

Seward, T.M., Henderson, C.M.B., Charnock, J.M., 2000. Indium(III) chloride complexing and solvation in hydrothermal solutions to 350°C: an EXAFS study. Chemical Geology, 167(1): 117-127.

Simons, B., Andersen, J.C.Ø., Shail, R.K., Jenner, F.E., 2017. Fractionation of Li, Be, Ga, Nb, Ta, In, Sn, Sb, W and Bi in the peraluminous Early Permian Variscan granites of the Cornubian Batholith: Precursor processes to magmatic-hydrothermal mineralisation. LITHOS, 278-281: 491-512.

Tischendorf, G., 2007. True and brittle micas: composition and solid-solution series. Mineralogical Magazine, 71(3): 285-320.

Tischendorf, G., Foerster, H.J., Gottesmann, B., 2001. Minor- and trace-element composition of trioctahedral micas; a review. Mineralogical Magazine, 65(2(429)): 249-276.

Tischendorf, G., Gottesmann, B., Foerster, H.-J., Trumbull, R.B., 1997. On Li-bearing micas; estimating Li from electron microprobe analyses and an improved diagram for graphical representation. Mineralogical Magazine, 61(6): 809-834.

Tott, K.A. et al., 2019. Ferromagnesian silicates and oxides as vectors to metamorphosed sediment- hosted Pb-Zn-Ag-(Cu-Au) deposits in the Cambrian Kanmantoo Group, South Australia. Journal of Geochemical Exploration.

U.S Geological Survey, 2020. Indium, U.S Geological Survey, U.S Geological Survey.

Wager, L.R., Smit, J.v.R., Irving, H., 1958. Indium content of rocks and minerals from the Skaergaard intrusion, East Greenland. Geochimica et Cosmochimica Acta, 13(2): 81-86.

Valkama, M., Sundblad, K., Cook, N., Ivashchenko, V., 2016a. Geochemistry and petrology of the indium-bearing polymetallic skarn ores at Pitkäranta, Ladoga Karelia, Russia. Mineralium Deposita, 51(6): 823-839.

Valkama, M., Sundblad, K., Nygård, R., Cook, N., 2016b. Mineralogy and geochemistry of indium-bearing polymetallic veins in the Sarvlaxviken area, Lovisa, Finland. Ore Geology Reviews, 75: 206-219.

Warren, M.R., Hanley, J.J., Ames, D.E., Jackson, S.E., 2015. The Ni–Cr–Cu content of biotite as pathfinder elements for magmatic sulfide exploration associated with mafic units of the Sudbury Igneous Complex, Ontario, Canada. Journal of Geochemical Exploration, 153: 11-29.

Winter, J.D., 2014. Principles of Igenous and Metamorphic Petrology. Pearson.

Volfinger, M., Robert, J.-L., 1980. Structural control of the distribution of trace elements between silicates and hydrothermal solutions. Geochimica et Cosmochimica Acta, 44(10): 1455-1461.

Appendix A.1 – Major elements for biotite, sample: KS1716, KS1710, KS1715

Meassurment	52	56	54	55	53	195	197	199	227	228	180	181	182	208	209	211
Sample	KS1716	KS1716	KS1716	KS1716	KS1716	KS1710	KS1710	KS1710	KS1710	KS1710	KS1715	KS1715	KS1715	KS1715	KS1715	KS1715
Granite type	Mustavaara	Mustavaara	Mustavaara	Mustavaara	Mustavaara	Mustavaara	Mustavaara	Mustavaara	Mustavaara	Mustavaara	Repomäki	Repomäki	Repomäki	Repomäki	Repomäki	Repomäki
Mica	Annite	Annite	Annite	Annite	Annite	Annite	Annite	Annite	Annite	Annite	Annite	Annite	Annite	Annite	Annite	Annite
SiO_2 [wt%]	31,66	31,53	31,21	31,36	30,05	35,52	30,21	31,94	31,59	30,46	31,15	31,10	30,78	30,50	31,65	31,00
Al_2O_3	11,45	11,64	11,58	11,86	11,89	11,17	12,49	12,29	11,25	13,12	16,00	15,11	14,81	14,25	14,49	14,59
FeO	36,16	36,40	36,74	36,43	37,58	31,57	37,86	36,04	36,61	39,78	34,79	35,40	35,92	36,80	35,15	36,11
MgO	2,06	1,96	2,04	1,86	2,11	3,87	3,38	3,43	3,47	2,17	0,25	0,26	0,26	0,25	0,27	0,26
ZnO	0,17	0,18	0,18	0,18	0,17	0,09	0,10	0,23	0,11	0,07	0,12	0,16	0,17	0,17	0,17	0,25
CaO	0,00	0,01	0,09	0,02	0,31	2,30	0,39	0,20	0,31	1,01	0,00	0,00	0,00	0,00	0,00	0,00
Na_2O	0,0791	0,08261	0,072	0,075	0,061	0,59	0,04	0,04	0,24	0,03	0,055	0,072	0,066	0,075	0,055	0,062
K_2O	8,50	8,52	8,38	8,51	7,98	6,26	5,35	7,62	6,81	5,51	8,97	9,03	8,78	8,53	8,48	8,70
TiO_2	3,46	3,23	3,25	3,28	3,38	2,22	3,75	1,77	3,20	1,35	1,68	1,89	2,25	2,49	2,55	2,01
MnO	0,24	0,25	0,26	0,20	0,24	0,26	0,27	0,24	0,24	0,34	0,30	0,39	0,40	0,42	0,38	0,50
Rb_2O	0,11	0,12	0,11	0,12	0,11	0,07	0,06	0,12	0,08	0,09	0,24	0,22	0,20	0,19	0,20	0,19
Li_2O	0,10	0,08	0,09	0,10	0,11	0,092	0,108	0,074	0,094	0,082	0,44	0,36	0,36	0,32	0,61	0,32
Total [%]	94,00	94,00	94,00	94,00	94,00	94,00	94,00	94,00	94,00	94,00	94,00	94,00	94,00	94,00	94,00	94,00
Si [apfu]	2,718	2,711	2,690	2,696	2,606	2,920	2,571	2,719	2,692	2,622	2,643	2,656	2,636	2,626	2,683	2,657
Al	1,158	1,179	1,176	1,202	1,215	1,082	1,253	1,234	1,130	1,331	1,600	1,520	1,494	1,445	1,448	1,474
Fe2+	2,596	2,618	2,648	2,620	2,725	2,170	2,694	2,566	2,609	2,864	2,468	2,527	2,572	2,649	2,492	2,588
Mg	0,263	0,251	0,262	0,239	0,273	0,474	0,429	0,435	0,441	0,278	0,032	0,033	0,033	0,032	0,034	0,033
Zn	0,011	0,012	0,012	0,011	0,011	0,006	0,006	0,015	0,007	0,004	0,007	0,010	0,011	0,011	0,011	0,016
Ca	0,000	0,001	0,008	0,002	0,029	0,202	0,036	0,018	0,028	0,093	0,000	0,000	0,000	0,000	0,000	0,000
Na	0,013	0,014	0,012	0,013	0,010	0,094	0,007	0,006	0,040	0,006	0,009	0,012	0,011	0,013	0,009	0,010
K	0,931	0,934	0,921	0,933	0,883	0,656	0,581	0,827	0,741	0,605	0,971	0,984	0,959	0,937	0,917	0,952
Ti	0,224	0,209	0,211	0,212	0,220	0,138	0,240	0,114	0,205	0,087	0,107	0,121	0,145	0,161	0,162	0,130
Mn	0,018	0,018	0,019	0,015	0,018	0,018	0,020	0,018	0,017	0,025	0,022	0,028	0,029	0,031	0,027	0,037
Rb	0,006	0,007	0,006	0,007	0,006	0,004	0,003	0,007	0,004	0,005	0,013	0,012	0,011	0,011	0,011	0,010
Li	0,033	0,029	0,032	0,034	0,037	0,030	0,037	0,025	0,032	0,028	0,149	0,125	0,124	0,111	0,209	0,111
^{IV}Al	1,282	1,289	1,310	1,304	1,394	1,080	1,429	1,281	1,308	1,378	1,357	1,344	1,364	1,374	1,317	1,343
^{VI}Al	-0,124	-0,110	-0,134	-0,102	-0,178	0,002	-0,176	-0,047	-0,178	-0,047	0,243	0,176	0,130	0,071	0,131	0,131
mgli	0,231	0,222	0,229	0,205	0,236	0,444	0,392	0,410	0,409	0,250	-0,117	-0,092	-0,091	-0,080	-0,175	-0,077
feal	2,961	2,954	3,012	2,948	3,142	2,324	3,130	2,744	3,009	3,023	2,354	2,500	2,616	2,770	2,551	2,623

Appendix A.2 – Major elements for biotite, sample: KS1718, KS1617

Meassurment	37	38	100	99	101	102	39	35	98	190	191	194
Sample	KS1718	KS1718	KS1718	KS1718	KS1718	KS1718	KS1718	KS1718	KS1718	KS1617	KS1617	KS1617
Granite type	Nietjärvi	Nietjärvi	Nietjärvi	Nietjärvi	Nietjärvi	Nietjärvi	Nietjärvi	Nietjärvi	Nietjärvi	Mosautodor	Mosautodor	Mosautodor
Mica	Annite	Annite	Annite	Annite	Annite	Annite	Annite	Annite	Annite	Siderophyllite	Siderophyllite	Siderophyllite
SiO_2 [wt%]	32,93	32,52	33,07	32,93	32,60	32,70	32,39	32,68	33,03	37,72	35,17	35,35
Al_2O_3	18,42	18,19	18,21	18,78	18,20	18,22	18,30	18,31	19,08	23,84	23,22	22,59
FeO	29,89	30,47	30,14	29,62	30,66	30,49	30,40	29,97	28,80	20,58	23,85	23,70
MgO	0,17	0,17	0,16	0,17	0,17	0,17	0,18	0,17	0,17	0,15	0,08	0,03
ZnO	0,15	0,15	0,18	0,18	0,18	0,18	0,16	0,16	0,18	0,07	0,08	0,08
CaO	0,00	0,00	0,00	0,00	0,00	0,00	0,00	0,00	0,02	0,01	0,01	0,00
Na_2O	0,13	0,12	0,14	0,13	0,14	0,14	0,09	0,10	0,10	0,07	0,08	0,11
K_2O	8,97	9,08	8,94	8,99	8,91	8,91	8,98	9,10	9,19	9,63	9,35	9,77
TiO_2	2,02	1,94	1,79	1,81	1,79	1,80	2,17	2,01	1,86	0,34	0,42	0,47
MnO	0,41	0,42	0,42	0,42	0,42	0,42	0,41	0,42	0,42	0,23	0,26	0,27
Rb_2O	0,20	0,20	0,20	0,21	0,20	0,22	0,25	0,35	0,35	0,43	0,45	0,53
Li_2O	0,713	0,736	0,734	0,752	0,737	0,746	0,665	0,732	0,807	0,932	1,029	1,106
Total [%]	94,00	94,00	94,00	94,00	94,00	94,00	94,00	94,00	94,00	94,00	94,00	94,00
Si [apfu]	2,693	2,674	2,708	2,689	2,680	2,686	2,663	2,682	2,689	2,881	2,751	2,773
Al	1,776	1,763	1,757	1,807	1,764	1,763	1,773	1,771	1,831	2,146	2,141	2,088
Fe2+	2,044	2,096	2,064	2,022	2,107	2,094	2,090	2,057	1,961	1,314	1,560	1,554
Mg	0,021	0,020	0,020	0,020	0,020	0,020	0,022	0,021	0,021	0,017	0,009	0,003
Zn	0,009	0,009	0,011	0,011	0,011	0,011	0,010	0,010	0,011	0,004	0,005	0,005
Ca	0,000	0,000	0,000	0,000	0,000	0,000	0,000	0,000	0,002	0,001	0,001	0,000
Na	0,021	0,019	0,022	0,020	0,022	0,022	0,014	0,016	0,016	0,011	0,012	0,016
K	0,935	0,952	0,934	0,936	0,934	0,933	0,942	0,953	0,955	0,938	0,932	0,977
Ti	0,124	0,120	0,110	0,111	0,111	0,111	0,134	0,124	0,114	0,019	0,025	0,028
Mn	0,028	0,029	0,029	0,029	0,030	0,029	0,029	0,029	0,029	0,015	0,017	0,018
Rb	0,010	0,011	0,011	0,011	0,011	0,012	0,013	0,018	0,018	0,021	0,023	0,027
Li	0,234	0,243	0,242	0,247	0,244	0,246	0,220	0,242	0,264	0,286	0,324	0,349
^{IV}Al	1,307	1,326	1,292	1,311	1,320	1,314	1,337	1,318	1,311	1,119	1,249	1,227
^{VI}Al	0,469	0,437	0,465	0,496	0,444	0,449	0,436	0,453	0,519	1,027	0,892	0,862
mgli	-0,214	-0,223	-0,222	-0,226	-0,223	-0,226	-0,198	-0,221	-0,244	-0,269	-0,314	-0,346
feal	1,727	1,808	1,738	1,667	1,804	1,786	1,817	1,757	1,584	0,321	0,710	0,738

Appendix A.3 – Major elements for biotite, sample: KS1626

Meassurment	76	77	133	132	134	135	73	136	75
Sample	KS1626	KS1626	KS1626	KS1626	KS1626	KS1626	KS1626	KS1626	KS1626
Granite type	Ristinoja	Ristinoja	Ristinoja	Ristinoja	Ristinoja	Ristinoja	Ristinoja	Ristinoja	Ristinoja
Mica	Siderophyllite	Siderophyllite	Siderophyllite	Siderophyllite	Siderophyllite	Siderophyllite	Siderophyllite	Siderophyllite	Siderophyllite
SiO_2 [wt%]	38,42	38,53	38,55	39,07	39,60	38,87	38,68	39,11	39,58
Al_2O_3	21,95	22,04	21,95	21,74	21,91	21,91	21,67	21,82	22,48
FeO	20,31	20,11	20,11	19,41	18,98	19,73	20,20	19,60	18,02
MgO	0,01	0,01	0,02	0,00	0,02	0,01	0,01	0,01	0,01
ZnO	0,16	0,15	0,16	0,15	0,15	0,15	0,15	0,15	0,16
CaO	0,00	0,00	0,00	0,00	0,00	0,00	0,00	0,00	0,00
Na_2O	0,19	0,18	0,16	0,20	0,14	0,18	0,20	0,19	0,18
K_2O	9,84	9,83	9,98	10,00	9,95	9,80	9,81	9,73	9,87
TiO_2	0,20	0,21	0,13	0,25	0,17	0,21	0,27	0,23	0,21
MnO	0,51	0,50	0,50	0,49	0,48	0,50	0,51	0,50	0,50
Rb_2O	0,54	0,54	0,57	0,59	0,59	0,57	0,59	0,57	0,57
Li_2O	1,88	1,88	1,86	2,10	2,01	2,08	1,92	2,09	2,40
Total [%]	94,00	94,00	94,00	94,00	94,00	94,00	94,00	94,00	94,00
Si [apfu]	2,937	2,941	2,946	2,971	2,998	2,957	2,955	2,970	2,975
Al	1,977	1,982	1,977	1,947	1,954	1,964	1,951	1,953	1,992
Fe2+	1,298	1,283	1,285	1,234	1,201	1,255	1,290	1,244	1,132
Mg	0,001	0,001	0,002	0,001	0,002	0,001	0,001	0,001	0,001
Zn	0,009	0,009	0,009	0,008	0,008	0,008	0,008	0,008	0,009
Ca	0,000	0,000	0,000	0,000	0,000	0,000	0,000	0,000	0,000
Na	0,028	0,027	0,024	0,029	0,021	0,027	0,029	0,028	0,026
K	0,960	0,957	0,973	0,970	0,960	0,951	0,956	0,943	0,947
Ti	0,012	0,012	0,007	0,014	0,010	0,012	0,016	0,013	0,012
Mn	0,033	0,033	0,032	0,032	0,031	0,032	0,033	0,032	0,032
Rb	0,027	0,027	0,028	0,029	0,029	0,028	0,029	0,028	0,027
Li	0,577	0,578	0,573	0,642	0,612	0,635	0,588	0,638	0,726
^{IV}Al	1,063	1,059	1,054	1,029	1,002	1,043	1,045	1,030	1,025
^{VI}Al	0,914	0,923	0,923	0,918	0,952	0,921	0,905	0,923	0,967
mgli	-0,575	-0,577	-0,571	-0,641	-0,609	-0,634	-0,588	-0,637	-0,725
feal	0,429	0,405	0,402	0,362	0,290	0,379	0,434	0,367	0,210

Appendix B.1 – Trace elements for biotite, samples: KS1716, KS1710, KS1715

Meassurment	52	56	54	55	53	195	197	199	227	228	180	181	182	208	209	211
Sample	KS1716	KS1716	KS1716	KS1716	KS1716	KS1710	KS1710	KS1710	KS1710	KS1710	KS1715	KS1715	KS1715	KS1715	KS1715	KS1715
Granite type	Mustavaara	Mustavaara	Mustavaara	Mustavaara	Mustavaara	Mustavaara	Mustavaara	Mustavaara	Mustavaara	Mustavaara	Repomäki	Repomäki	Repomäki	Repomäki	Repomäki	Repomäki
Mica	annite	Annite	Annite	Annite	Annite	Annite	Annite	Annite	Annite	Annite	Annite	Annite	Annite	Annite	Annite	Annite
Li [ppm]	442	394	434	460	494	428	502	342	437	379	2024	1688	1674	1492	2841	1492
B	17,27	13,96	6,93	10,76	9,82	14,53	17,07	7,99	12,79	19,13	6,04	b.d	6,13	4,47	8,60	6,73
P	113	97	243	159	811	2866	191	114	151	812	163	147	156	128	131	167
Sc	19,09	18,92	24,78	19,57	29,26	35,13	76,28	21,56	48,47	36,25	25,54	25,65	24,81	25,01	24,88	24,71
V	52,96	48,70	58,08	52,44	59,77	58,26	124,05	36,20	109,62	30,79	3,56	3,34	3,19	3,87	3,02	3,30
Cr	32,37	26,61	36,31	13,36	34,55	35,14	80,66	11,06	61,08	10,82	0,33	0,36	b.d	0,30	0,15	b.d
Co	17,94	17,14	15,88	17,28	16,34	14,64	14,35	21,84	17,67	11,43	2,78	3,03	2,38	3,39	3,57	2,98
Ni	15,73	16,59	12,62	14,29	11,57	22,39	22,66	27,92	24,34	22,06	b.d	b.d	b.d	b.d	b.d	b.d
Cu	0,62	0,80	1,74	0,80	4,31	11,22	23,28	3,39	19,08	27,16	3,42	0,59	2,07	1,08	8,16	b.d
Zn	1370	1473	1455	1444	1337	745	785	1871	874	525	939	1324	1350	1332	1353	2003
Ga	65,40	67,71	65,27	63,09	65,83	86,91	86,74	63,81	71,44	89,79	163	159	159	153	147	148
Ge	3,73	4,19	4,58	4,82	3,79	5,32	4,32	5,72	6,57	5,54	9,59	8,90	7,72	7,08	6,51	6,35
Rb	1018	1076	1045	1110	998	618	524	1102	695	807	2149	2043	1856	1775	1823	1722
Sr	0,70	1,07	0,90	0,95	1,58	11,89	8,67	6,89	5,34	15,21	0,19	0,11	0,15	0,16	0,32	0,07
Y	0,37	1,65	15,34	3,56	61,64	318,52	95,20	67,78	54,93	178,50	0,55	0,24	0,45	0,26	4,87	0,44
Zr	0,77	1,09	2,09	0,70	2,45	12,46	26,74	1,23	26,15	11,41	1,52	1,48	1,56	1,96	6,12	2,01
Nb	319	309	336	384	357	147	219	194	179	141	564	519	529	548	550	547
Mo	1,41	1,73	1,16	2,29	0,99	0,44	3,02	0,87	1,69	0,49	8,54	7,17	6,37	6,36	9,10	7,78
In	0,25	0,26	0,30	0,27	0,34	0,22	0,52	0,38	0,37	0,65	0,83	1,03	1,09	1,14	1,08	1,21
Sn	13,20	14,09	14,29	16,18	14,39	8,76	26,51	17,94	17,85	55,02	132	110	98,17	84,31	82,91	89,57
Sb	b.d	0,03	b.d	b.d	b.d	b.d	b.d	0,10	b.d	b.d	0,06	0,06	b.d	b.d	b.d	0,17
Cs	24,34	34,48	47,30	55,92	36,85	25,25	29,97	61,59	42,10	56,49	42,32	29,23	31,70	25,14	41,34	19,78
Ba	1061	841	900	736	863	515	433	1046	504	626	26,79	24,23	24,16	26,09	23,90	24,05
Ce	0,08	0,53	6,03	1,93	22,18	1704,38	1436,62	756,64	716,40	1649,06	0,36	0,07	0,17	0,15	2,80	0,18
Hf	0,11	0,09	0,31	0,06	0,20	0,56	1,16	0,17	1,03	0,52	0,37	0,34	0,37	0,52	0,57	0,30
Ta	10,87	11,56	12,70	14,14	12,40	4,89	3,89	12,00	3,57	7,63	65,40	41,74	33,55	27,62	28,60	31,35
W	0,48	0,16	0,45	0,32	0,22	b.d	7,67	b.d	2,35	0,61	1,36	1,24	1,40	1,38	2,26	2,73
Tl	6,03	5,74	6,10	6,79	5,76	3,66	3,91	7,40	4,42	5,64	12,92	11,97	11,27	10,33	10,57	10,92
Pb	3,88	6,01	5,96	4,44	9,08	44,12	146,95	30,61	83,85	46,48	5,67	4,11	4,15	4,16	4,71	4,14
Bi	b.d	0,036	0,047	0,027	0,013	0,073	1,42	0,04	1,29	b.d	0,011	0,040	0,050	0,048	0,043	0,010

Appendix B.2 – Trace elements for biotite, samples: KS1718, KS1617

Meassurment	37	38	100	99	101	102	39	35	98	190	191	194
Sample	KS1718	KS1718	KS1718	KS1718	KS1718	KS1718	KS1718	KS1718	KS1718	KS1617	KS1617	KS1617
Granite type	Nietjärvi	Nietjärvi	Nietjärvi	Nietjärvi	Nietjärvi	Nietjärvi	Nietjärvi	Nietjärvi	Nietjärvi	Mosautodor	Mosautodor	Mosautodor
Mica	Annite	Annite	Annite	Annite	Annite	Annite	Annite	Annite	Annite	Siderophyllite	Siderophyllite	Siderophyllite
Li [ppm]	3311	3418	3412	3492	3423	3463	3089	3402	3749	4332	4780	5139
B	8,78	b.d	9,47	7,58	b.d	6,72	b.d	9,24	b.d	34,31	41,51	6,44
P	119	117	107	97,30	101	105	122	131	119	170	157	165
Sc	15,23	15,06	15,38	14,77	15,05	14,28	16,52	15,35	15,89	27,54	27,19	25,94
V	1,25	1,17	0,88	1,20	1,02	1,16	1,39	1,47	1,03	0,29	0,22	0,30
Cr	0,10	0,05	b.d	b.d	b.d	0,23	0,09	b.d	b.d	b.d	0,24	0,25
Co	2,06	1,86	1,73	1,65	1,49	1,65	1,49	1,38	1,54	1,61	2,08	2,80
Ni	1,68	2,18	b.d	4,39	2,73	b.d	2,79	2,79	b.d	1,02	b.d	b.d
Cu	5,47	1,32	2,60	4,17	1,14	1,02	8,13	2,97	4,35	32,33	35,93	3,50
Zn	1227	1227	1419	1413	1408	1421	1267	1287	1408	567	654	634
Ga	173	172	172	174	171	171	174	174	174	194	198	180
Ge	6,29	6,38	7,08	6,36	6,48	6,33	6,64	7,10	8,59	10,75	9,83	8,64
Rb	1822	1856	1825	1954	1849	1998	2319	3204	3188	3934	4119	4843
Sr	0,20	0,07	0,09	0,52	0,08	0,12	0,38	0,16	0,22	1,43	1,41	0,14
Y	2,69	1,13	1,64	3,98	1,00	1,48	8,07	3,00	15,42	156	231	12,10
Zr	1,84	1,05	1,33	5,42	0,99	1,13	7,50	1,44	32,86	267	373	21,90
Nb	612	694	755	844	705	677	776	651	994	590	713	664
Mo	3,00	2,33	3,24	2,33	2,89	2,67	2,22	2,47	1,38	2,68	0,90	0,46
In	0,42	0,42	0,40	0,43	0,40	0,40	0,42	0,44	0,42	0,20	0,15	0,12
Sn	173	174	179	181	175	176	174	177	190	37,02	32,73	29,70
Sb	b.d	b.d	b.d	b.d	0,20	b.d	b.d	0,19	b.d	b.d	0,20	0,18
Cs	17,53	18,03	16,16	22,66	17,80	23,83	35,06	165	110	103	121	111
Ba	14,85	15,05	14,60	14,66	16,03	10,52	20,65	24,90	23,83	16,42	12,99	2,54
Ce	3,60	1,66	1,87	3,78	0,69	0,78	14,11	3,55	7,63	11,75	40,91	1,15
Hf	0,54	0,41	0,35	0,59	0,39	0,44	1,38	0,69	1,97	25,25	37,65	2,49
Ta	27,84	39,80	44,16	55,50	37,58	32,89	38,84	47,33	75,55	80,90	107	114
W	1,36	0,78	0,70	1,54	0,78	1,22	3,85	5,19	4,63	23,12	25,90	14,98
Tl	11,59	12,01	10,95	11,74	11,69	11,70	14,47	16,25	15,85	14,20	15,10	19,05
Pb	7,51	8,38	7,38	8,66	8,11	8,46	10,36	8,38	8,80	15,63	12,33	3,46
Bi	0,036	b.d	b.d	0,023	0,013	b.d	0,022	0,006	b.d	b.d	0,18	0,037

Appendix B.3 – Trace elements for biotite, sample: KS1626

Meassurment	76	77	133	132	134	135	73	136	75
Sample	KS1626	KS1626	KS1626	KS1626	KS1626	KS1626	KS1626	KS1626	KS1626
Granite type	Ristinoja	Ristinoja	Ristinoja	Ristinoja	Ristinoja	Ristinoja	Ristinoja	Ristinoja	Ristinoja
Mica	Siderophyllite	Siderophyllite	Siderophyllite	Siderophyllite	Siderophyllite	Siderophyllite	Siderophyllite	Siderophyllite	Siderophyllite
Li [ppm]	8714	8746	8663	9754	9339	9640	8898	9700	11160
B	15,19	8,42	15,45	13,93	22,17	11,20	11,43	12,99	19,42
P	133	114	150	137	142	116	108	126	110
Sc	22,47	21,41	21,15	22,24	20,53	21,58	21,89	21,66	15,91
V	0,11	0,08	0,03	0,03	b.d	b.d	b.d	0,03	b.d
Cr	0,20	b.d	0,07	0,27	0,06	0,26	0,32	0,25	b.d
Co	0,80	0,50	0,27	0,63	0,43	0,57	0,39	0,37	0,80
Ni	0,48	2,48	b.d	1,96	b.d	b.d	b.d	1,13	b.d
Cu	0,92	b.d	2,84	b.d	4,64	b.d	b.d	b.d	2,74
Zn	1273	1231	1274	1182	1208	1182	1207	1177	1286
Ga	174	170	182	197	184	177	210	181	163
Ge	5,95	5,33	6,77	6,88	4,85	7,59	6,98	7,80	4,34
Rb	4936	4955	5227	5351	5381	5237	5360	5247	5190
Sr	0,13	0,03	0,19	b.d	0,25	0,03	0,05	b.d	0,10
Y	8,91	0,50	13,37	0,21	12,37	1,52	1,01	0,21	7,72
Zr	45,24	1,16	62,00	0,25	51,06	8,44	1,99	0,37	37,86
Nb	271	262	304	560	343	474	483	538	262
Mo	0,76	0,97	0,67	0,64	1,27	1,06	0,44	0,64	0,65
In	0,39	0,39	0,38	0,38	0,38	0,39	0,42	0,40	0,29
Sn	392	383	362	375	309	356	373	370	219
Sb	b.d	b.d	b.d	b.d	b.d	0,25	b.d	b.d	0,18
Cs	140	160	237	480	328	415	411	468	437
Ba	4,88	0,60	4,05	0,76	5,84	1,40	0,57	0,87	2,14
Ce	5,80	0,17	17,33	0,10	16,78	1,96	0,89	0,08	6,45
Hf	3,74	0,16	6,59	0,11	4,74	0,96	1,00	0,20	4,25
Ta	110	78,23	76,18	116	84,82	111	109	116	68,54
W	25,52	21,28	21,86	20,33	17,32	15,06	13,91	20,62	13,35
Tl	16,77	17,31	19,86	19,81	18,54	18,18	18,25	18,71	18,09
Pb	8,62	7,73	12,77	9,24	14,24	9,58	8,62	8,84	7,06
Bi	0,028	0,13	b.d	b.d	0,056	0,078	0,055	b.d	b.d

Appendix C

*Table 4. Unpublished bulk rock chemistry data. *Biotite abundance % estimated by Metso (2018). (K. Sundblad, in prep.)*

	Zr/Hf	Rb/Ba	Nb/Ta	Zn [ppm]	Sn [ppm]	Mo [ppm]	In [ppm]	W [ppm]	Cu [ppm]	F [ppm]	Nb [ppm]	Ta [ppm]	*Biotite %
KS1710	40.0	0.16	11.67	80	3	<2	<0.2	2	<10	0.02	21	1.8	10
KS1716	41.3	0.22	12.72	60	5	<2	<0.2	2	<10	0.08	14	1.1	3
KS1715	23.1	2.77	11.69	90	7	2	<0.2	2	<10	0.30	69	5.9	9
KS1718	16.5	17.3	8.75	60	10	<2	<0.2	2	<10	0.31	49	5.6	5
KS1617	10.4	21.8	3.70	<30	1	<2	<0.2	5	<10	0.14	44	11.9	5
KS1626	9.71	102.5	1.74	40	12	<2	<0.2	3	<10	0.27	27	15.5	5